Neural Networks 190 (2025) 107624

Contents lists available at ScienceDirect

Neural Networks

journal homepage: www.elsevier.com/locate/neunet

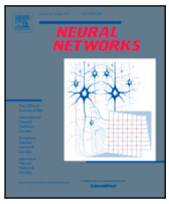

Full Length Article

HyTract: Advancing tractography for neurosurgical planning with a hybrid method integrating neural networks and a path search algorithm

Mateusz Korycinski [a,*], Konrad A. Ciecierski [a], Ewa Niewiadomska-Szynkiewicz [b]

[a] Department of Artificial Intelligence Applications in Medicine and Sensitive Data Analysis, NASK National Research Institute, Kolska 12, Warsaw, 01-045, Poland
[b] Institute of Control and Computation Engineering, Warsaw University of Technology, Nowowiejska 15/19, Warsaw, 00-665, Poland

ARTICLE INFO

Keywords:
Tractography
Artificial neural networks
DTI
MRI
Path search

ABSTRACT

The advent of advanced MRI techniques has opened up promising avenues for exploring the intricacies of brain neurophysiology, including the network of neural connections. A more comprehensive understanding of this network provides invaluable insights into the human brain's underlying structural architecture and dynamic functionalities. Consequently, determining the location of the neural fibers, known as tractography, has emerged as a subject of significant interest to both basic scientific research and practical domains, such as preoperative planning. This work presents a novel tractography method, HyTract, constructed using artificial neural networks and a path search algorithm. Our findings demonstrate that this method can accurately identify the location of nerve fibers in close proximity to the surgical field. Compared with well established methods, tracts computed with HyTract show Mean Euclidean Distance of 9 or lower, indicating a good accuracy in tract reconstruction. Furthermore, its architecture ensures the explainability of the obtained tracts and facilitates adaptation to new tasks.

1. Introduction

Tractography is an important area of neurobiology. The utilization of non-invasive medical imaging techniques, such as Magnetic Resonance Imaging (MRI), allows the delineation of an intricate tissue organization, including that of the brain (Pooley, 2005). This encompasses the topology of the neural tracts, which are bundles of axons connecting neurons to form sophisticated neural networks, thus facilitating the high-level functioning of the brain.

The brain's anatomy can be investigated via T1 and T2-weighted MRI sequences. However, these imaging techniques only allow visualization of a limited set of features, such as gray and white matter or some pathological states. Other MRI modalities can depict additional features, e.g., allowing the identification of myocardial fibrosis from 3D cardiac MRI (CMR) (Mehrnia et al., 2024), visualization of functional cortex areas (Logothetis, Pauls, Augath, Trinath, & Oeltermann, 2001; Singleton, 2009) with functional MRI (fMRI), or the projection of all neural connections within the brain with Diffusion-weighted imaging (DWI) (Hagmann et al., 2006). In particular, the Diffusion Tensor Imaging (DTI) model, as described in Basser, Mattiello, and LeBihan (1994), is a widely used clinical setup.

By employing a diverse array of techniques to examine diffusion signal, it is possible to ascertain the direction of water diffusion within each voxel representing the brain volume in three-dimensional space. Given the anatomy of neural cells, this reflects the organization of axons. Bundles of these structures constitute a neural tract, which is defined as a structural connection between brain regions that provides a means for electrical signal transduction. The totality of such connections within the brain is referred to as a tractogram. It is comprised of a set of strands in three-dimensional space, defined as streamlines, which represent bundles of axons.

The information provided by these MRI modalities and their interpretation models helps to build a comprehensive view of the structural and functional connections between different areas of the brain. Investigating these is of interest to scientists engaged in basic research, as it allows them to study networks responsible for various aspects of our lives, including movement of limbs, cognition, memory formation, and many others. At the same time, such neural tract reconstruction is of practical use. One example is preoperative planning prior to the neurosurgeries involving tumor mass resection.

Although such surgeries are life-saving for many gliomas (Przybylowski, Hervey-Jumper, & Sanai, 2021; Yousefi et al., 2022), they are invasive, particularly when the tumor infiltrates significant cortical regions. Damaging these during an intervention can impair the patient's motor or cognitive functions (Chaichana et al., 2014; Sanai, Polley, McDermott, Parsa, & Berger, 2011). In addition, it is essential to keep

* Corresponding author.
E-mail address: mateusz.korycinski@nask.pl (M. Korycinski).

https://doi.org/10.1016/j.neunet.2025.107624
Received 4 July 2024; Received in revised form 21 March 2025; Accepted 12 May 2025
Available online 29 May 2025
0893-6080/© 2025 The Authors. Published by Elsevier Ltd. This is an open access article under the CC BY-NC-ND license (http://creativecommons.org/licenses/by-nc-nd/4.0/).

their inferent and afferent connections unimpaired, as damage to such can have similar effects as damaging cortex regions themselves. To partially address this issue, resection can be performed in multiple surgeries. Only a portion of the tumor mass is removed during the initial surgery to preserve critical structures. Due to the brain's plasticity, the remainder can be removed in subsequent attempts. It has been demonstrated that these regions can shift slightly on the brain's cortex over time, allowing surgeons to remove more infiltrated tissue (Duffau, 2008).

One of the most crucial aspects of this perspective is the precise localization of white matter fibers. Numerous tractography methods have been developed to achieve this objective, yet they provide a varying probability level. Moreover, the input of a trained radiology specialist is indispensable. Based on anatomical knowledge and expertise, such an expert can assess the topology of nerve fibers with greater assurance than using a single method alone. In addition to the concerns above regarding precision, these methods typically necessitate multiple preprocessing and fine-tuning steps, rendering them inaccessible to neurosurgeons.

An accurate comprehension of the patient's brain connectivity is of paramount importance when planning and performing neurosurgery. To enhance tractography accessibility for physicians specializing in areas other than radiology, a hybrid model integrating an artificial neural network and a path search algorithm has been proposed. This model is capable of accurately locating nerve fibers with high probability using DWI MRI data. By leveraging the artificial neural network for DWI MRI data analysis, the number of preprocessing steps required is reduced. With the successful implementation of this model, the system will be able to project the location of critical cortical regions based on functional MRI data and adjacent neural connections based on the tractography results, thus facilitating the planning and execution of the surgical intervention.

The main contributions of this work are summarized as follows.

1. We propose a novel approach to preparing a tractography training dataset through the computation of consensus tractograms. These are computed from several tractograms prepared with various methods for the same set of starting points. The consensus tractogram contains only streamlines (fibers, tracts) confirmed by all the methods employed. The confirmation is given by measuring pairwise similarity between fibers computed with different methods.
2. In order to compute a consensus tractogram, it is necessary to employ a measure that can be used to compare two tractograms. Such measures are available for abstract graphs derived from tractography (Bukhari et al., 2022; Fornito, Zalesky, & Breakspear, 2013), but not for comparing individual streamlines themselves. In this work, we propose to use the mean Euclidean distance between streamline key points as a measure of similarity.
3. To compute the topology of neural tracts, we assemble a hybrid method consisting of a custom lightweight neural network and a heuristic variant of the path search algorithm. The neural network is employed to analyze the diffusion signal and construct a weighted graph of possible structural connections within the brain. A heuristic A* algorithm is implemented to construct a tractogram based on this graph. The method does not necessitate meticulous data preprocessing and enables the visualization of the graph that serves as the foundation for the determined fibers. Given its hybrid nature, we name the method HyTract for Hybrid Tractography.

The remaining of the paper is organized as follows. Section 2 discusses related works divided into formal signal analysis methods and machine learning approaches. The research problem is presented in Section 3, which is followed by a detailed description of our HyTract method in Section 4. Section 5 introduces a novel concept of a consensus tractogram and explains in detail how such tractograms were prepared for training HyTract ANN. Implementation and training of the neural network are described in Section 6. This section presents experiments designed to choose the best architecture and training parameters. Experimental results with tract reconstruction and comparison with other available methods are provided in Section 7. The paper is concluded with a discussion in Section 8.

2. Related works

Computer algorithms are widely used for medical data analysis, including medical imaging. Many algorithms have been designed for EEG signal processing (Luján, Jimeno, Mateo Sotos, Ricarte, & Borja, 2021), or even the generation of a simulated EEG signal to ease the development and testing of new algorithms or hypotheses (Yektaeian Vaziri, Makkiabadi, & Samadzadehaghdam, 2023). Convolutional Neural Networks (CNN), which have been applied to various image processing problems (Adnan & Abdulbaqi, 2022; Agnihotri, Saraf, & Bapnad, 2019; Seydi et al., 2024), play a crucial role in radiology, easing the work of radiologists (Al-Yasriy, Al-Husieny, Mohsen, Khalil, & Hassan, 2020; Che, Brown, Foran, Nosher, & Hacihaliloglu, 2021; Milletari et al., 2017). Even low-resolution images are not an obstacle, as they proved to work well in such cases (Ganj, Ebadpour, Darvish, & Bahador, 2023).

Various computer algorithms have also been used to analyze DWI imaging. Basser, an inventor of DTI imaging, observed that a trajectory of the tract is parallel to the eigenvector associated with the largest eigenvalue of the local diffusion tensor (Basser, 1998; Basser et al., 1994). This observation allowed for the first visualization of the tract. Lazar et al. (2003) employed not only the eigenvector of the largest eigenvalue but also the information carried by the entire diffusion tensor. This algorithm, designated TEND, employs the tensor deflection technique. It utilizes a stopping criterion that blocks tract expansion when fractional anisotropy drops below a specified value or when the direction of the trajectory changes by more than 45°. Descoteaux et al. proposed in their study (Descoteaux, Deriche, Knösche, & Anwander, 2009) to apply sharpening deconvolution transform (SDT) of the diffusion orientation distribution function (ODF) from Q-ball imaging (Tuch, 2004) to obtain the fiber ODF (fODF). The transform revealed new insights into the relationship between the High Angular Resolution Diffusion Imaging (HARDI) signal, diffusion ODF, and the fODF. The sparsity of the fODF and the discrepancy between the Q-ball and the actual diffusion direction necessitate the utilization of a sharpening operation.

MRtrix3 (Tournier et al., 2019) is a freely available collection of methods for diffusion data processing and visualization. It implements global tractography using a multi-tissue spherical convolution model, introduced by Christiaens et al. (2015), extending the method proposed by Reisert et al. (2011) to be used with multi-shell response functions. Additionally, it enables the utilization of constrained spherical deconvolution, as described in the work of Tournier, Calamante, and Connelly (2007), which permits the estimation of the fODF. MRtrix incorporates algorithms that employ the fODF function to compute both deterministic and probabilistic tractograms, as detailed in Tournier, Calamante, and Connelly (2012).

Similarly to MRtrix3, DIPY (Garyfallidis et al., 2014) provides Python developers with a plethora of algorithms for tractography. This library contains implementations of signal interpretation methods, such as Constant Solid Angle (CSA) or Constrained Spherical Deconvolution (CSD). The signal interpretations generated by these models can be explored to compute tracts with many algorithms available, including EuDX (Garyfallidis, 2012), Closest Peak Direction Getter (CPDG), or Deterministic Maximum Direction Getter (DMDG) (Garyfallidis et al., 2014). Furthermore, it provides numerous methods for conducting preprocessing and postprocessing steps. With the use of the FURY package (Garyfallidis et al., 2021), it also allows to visualize tractograms interactively.

Given that such neural tracts can be conceptualized as a path in the graph representing all anatomical connections within the brain's white matter, a group of researchers decided to use path search algorithms for tracking by applying some modifications to the Djikstra's algorithm (Dijkstra, 1959). Andrew Zalesky proposed a method for tracking neural fibers by identifying the shortest path in a weighted digraph, as described in Zalesky (2008). In this approach, a single voxel is represented as a vertex with edges for all surrounding neighboring voxels. The weights of the edges are computed using a Bayesian framework, reflecting the alignment with fiber trajectories in the vicinity. Sotiropoulos, Bai, Morgan, Constantinescu, and Tench (2010) proposed a similar approach that demonstrated good accuracy for tracking crossing fibers. In such areas, voxels contain multiple fiber orientations, which presents a challenge for propagating the current trajectory in a direction that aligns with the underlying anatomical truth. The method proposed by the authors employs ODFs derived from Q-ball imaging (Tuch, 2004) and considers multiple fiber populations occurring within a single voxel (if partial volume exists). The image is treated as a multigraph, enabling the distribution of connectivities in a weighted manner, with the most probable tract obtaining the highest weight. Such methods could be enhanced with a novel cost definition for the graph edge proposed in Aronis, Delibasis, Fanariotis, and Maglogiannis (2016). It acknowledges a tract curvature and its alignment with the diffusion vector field by considering three terms calculated from the vector field. Minimizing these favors the smoothness of the calculated tracts and ensures that the transition between the current node and the candidate nodes is as parallel as possible with the diffusion eigenvectors.

The utilization of machine learning techniques offers a distinct advantage over classical mathematical models. This approach enables the estimation of local tissue propensities directly from raw diffusion data, thus facilitating neural fiber tracking without the need to use models for obtaining ODF or similar functions of the tensor field. The initial method of this nature was proposed by Neher et al. in Neher, Côté, Houde, Descoteaux, and Maier-Hein (2017) and Neher, Götz, Norajitra, Weber, and Maier-Hein (2015). This algorithm builds streamlines in a stepwise fashion, with a random forest classifier assigning probabilities to each of the directions available at a given point, along with the probability for the fiber termination. Tracking is terminated when the termination probability exceeds the cumulative sum of other probabilities.

Poulin et al. in Poulin et al. (2017) used classical feedforward and recurrent neural networks. The feedforward network outputs a set of three-dimensional vectors for each point in the diffusion data, which is analogous to the ODF function described above. The recurrent network, on the other hand, considers information observed in the voxels preceding the current one in relation to the entire fiber orientation. An extension of this approach was published in Poulin, Rheault, St-Onge, Jodoin, and Descoteaux (2018), where the recurrent network is used in a bundle-wise manner. This resulted in improved tracking efficacy, a higher number of valid streamlines, and better volume coverage compared to other methods.

Another method, named DeepTract, was proposed by Benou et al. in Benou and Riklin-Raviv (2018). It employs recurrent neural networks to estimate the local fiber orientation as a discrete probability density function. This allows us to sample the direction for fiber extension from a given point. The classification task in this method is similar to that of a random forest classifier proposed by Neher et al.

3. Problem formulation

The objective of this study is to develop a method for computing a tractogram based on the data available from the diffusion-weighted Imaging (DWI) experiment. A tractogram T is a set of streamlines, $T = (S^1, S^2, \dots, S^n)$, representing axonal bundles that constitute the structural connections within the brain. A streamline is a sequence of consecutively connected points $S^i = (s^i_1, s^i_2, \dots, s^i_{k_i})$, where k_i is the length of a streamline, $s^i_j = [x^i_j, y^i_j, z^i_j]$, $i = 1, \dots, n$, and s^i_j is the center of the jth voxel, where $j = 1, \dots, k_i$.

The first challenge to be addressed is the interpretation of the DWI data. DWI is an MRI technique where the whole brain volume is recorded with varying magnetic field gradients. A gradient describes the decay of the magnetic field strength along a given direction and, as a consequence, allows the measurement of the strength of the water diffusion along this axis. The DWI data comprise two parts. The first is the gradient table $G \in \mathbb{R}^{3\times L}$ describing the non-homogeneous magnetic field and its strength utilized in the data acquisition in L consecutive frames. The second part is the registered DWI data for the whole brain volume, i.e., $\Omega \in \mathbb{R}^{d_x \times d_y \times d_z \times L}$, where d_x, d_y, and d_z denote the dimensions of the recorded brain volume. The recorded signal does not directly contain information about the arrangement of axonal bundles (neural tracts). A dedicated algorithm has to be applied to compute the main water diffusion direction for each voxel, which, based on anatomical knowledge, translates into the location and orientation of axonal bundles (structural connections) within the white matter.

The second challenge is to utilize this information to compute neural tracts. This process is referred to as tracking and is typically conducted iteratively. Tracking commences with the establishment of a set of seed points, which are presumed to be the origin of neural fibers. Given the tissue organization within the brain, these are typically situated at the interface between the gray and white matter. Neural tracts, represented as streamlines in three-dimensional space, are extended in a stepwise manner based on the underlying interpretation of the diffusion-weighted imaging (DWI) signal until the stopping criterion is met.

Despite the advantages of existing tractography methods, they have certain limitations. Formal methods use termination thresholds related to the tissue properties derived from the underlying model for diffusion signal interpretation. Consequently, they are prone to premature termination when faced with regions of low anisotropy. Many probabilistic methods have a high rate of false positives due to data inadequacies. Some of these are addressed by machine learning techniques, where an artificial neural network can learn to handle some of the data defects. However, these architectures are typically immense, which makes them challenging to train. Moreover, their results are finished streamlines, with no information allowing for the reasoning behind elucidating them to be understood. This is a significant disadvantage in medical applications, where explainability is critical. It would be desirable for neurosurgical planning to either compute tracts with multiple methods or to invest more effort in time-consuming data preprocessing to limit the number of false positives, which can limit the area to conduct surgery. Therefore, a method that addresses these problems is required.

4. Overview of the HyTract method

This work introduces a novel hybrid approach to tractography, which combines signal processing with an artificial neural network (ANN) and a path search with a heuristic A* algorithm. A schematic view of this idea is presented in Fig. 1.

Tracking starts with a seed point given by the user and consists of three phases:

1. Initialization. DWI data is processed in small cuboid chunks of the measured brain volume $B^{\Theta\times\Theta\times\Theta\times L}$, where $B \in \Omega$, $\Theta \in \mathbb{N}$ is an odd value, $\Theta \geq 5, \Theta \leq min(d_x, d_y, d_z)$, and $[d_x, d_y, d_z]$ are the dimensions of the whole recorded brain volume. This cuboid chunk is picked from the DWI volume with the seed point positioned at the central voxel.
2. ANN processing. The artificial neural network model processes DWI data (the input tensor B and the gradient table G) and outputs a tensor $O \in \mathbb{R}^{\Theta\times\Theta\times\Theta}$ of probabilities p^i_j, describing how likely it is, that a jth voxel belongs to the streamline S^i. This way, ANN analyzes only the immediate vicinity of the streamline being elongated.

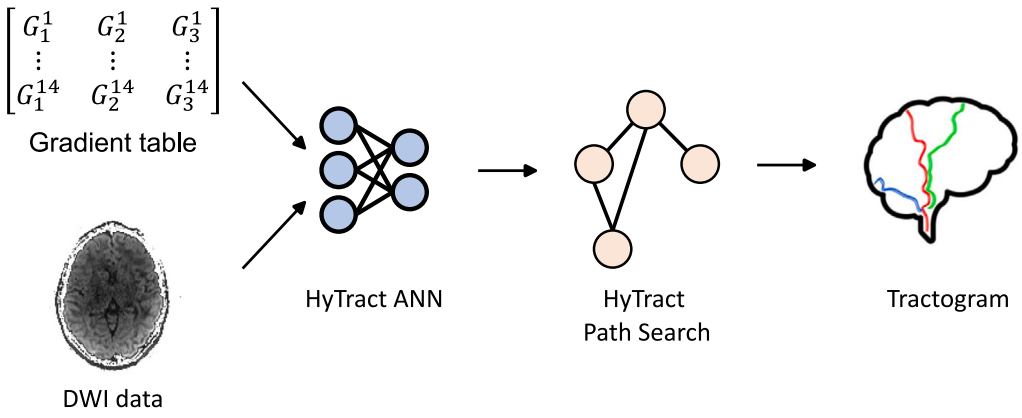

Fig. 1. The outline of the HyTract method.

3. Streamline elongation. A streamline is elongated from the central voxel to border targets in a cuboid chunk B using the heuristic A* algorithm, where voxels center are the graph nodes and edge costs are $1 - p_j^i$, $i = 1, \ldots, n$, and $j = 1, \ldots, k$. A border target is a voxel of the cuboid chunk B, for which the probability $p \geq \tau$, where τ is the threshold value determined by the user. Upon reaching the border, a designated border voxel is selected as the central voxel for the subsequent cube.

Utilization of small cuboid chunks at the time allows us to keep a small number of neurons in the ANN model. Moreover, for local tractography (e.g., near the surgical field), does not require to analyze the whole recorded brain volume. The tractogram is generated upon completion of the tracking process for all requested seed points. The following sections provide a more detailed description of the designed ANN models and the implementation of the heuristic A* algorithm.

4.1. HyTract ANN

We approached the designing of a neural network model with progressive refinement. We aimed to start with a simple shallow architecture to gradually increase complexity till we reach the optimal balance between accuracy and efficiency. Such an approach is particularly important for medical applications due to the high stakes of diagnostic accuracy, the complexity of medical data, and limited computational resources. Moreover, employing simple models that do not require significant computational power is essential to create sustainable AI with a smaller carbon footprint. As a result of this effort, a number of neural network architectures were crafted to generate input for a path search algorithm. The architecture that yielded the most promising outcomes, illustrated in Fig. 2, establishes a benchmark for reference. Divergent models vary in their approaches to processing input data, as depicted in the array of architectures showcased in Fig. 3. All configurations are capable of handling a cube sample with a side length of Θ, where Θ is an odd number and $\Theta \geq 5$. For clarity, all figures reference the scenario where $\Theta = 5$, chosen as the initial test cube size. In our analysis, we elected to include not only the DWI signal but also a gradient table, as it delineates the gradient utilized in the measurements.

In the Minimal Model (MM, Fig. 3A), a flattened vector of the DWI sample (cuboid chunk) is combined with a gradient table to create a single one-dimensional input vector that is processed by a single fully connected (FC) layer with ReLu activation. In contrast, the Dual Input Model (DIM, Fig. 3b) replaces the input layer with two independent fully connected (FC) layers, each processing one modality with a separate set of weights. The resulting tensors are then concatenated and passed to a hidden layer. The DIM model with weights (DIM-w, Fig. 3C) assumes input processing in the same manner as the DIM model.

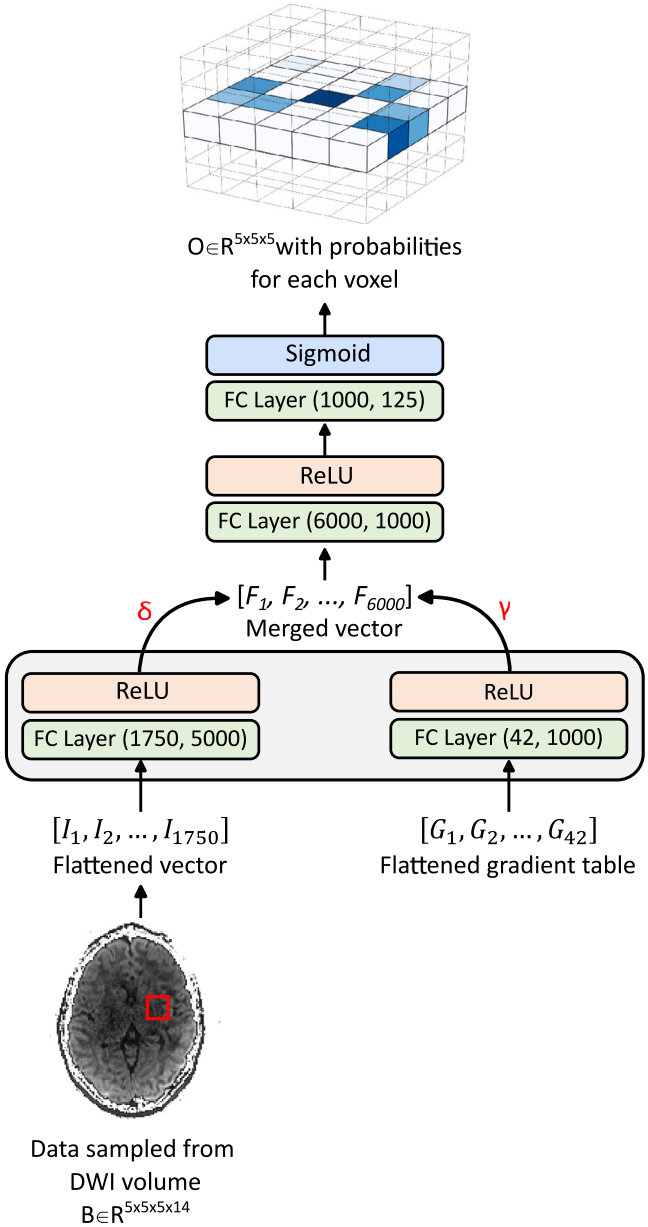

Fig. 2. Dual Input Model with importance weights (DIM-w) for $\Theta = 5$ and $L = 14$; $I_1, I_2, I_3, \ldots$ are elements of B.

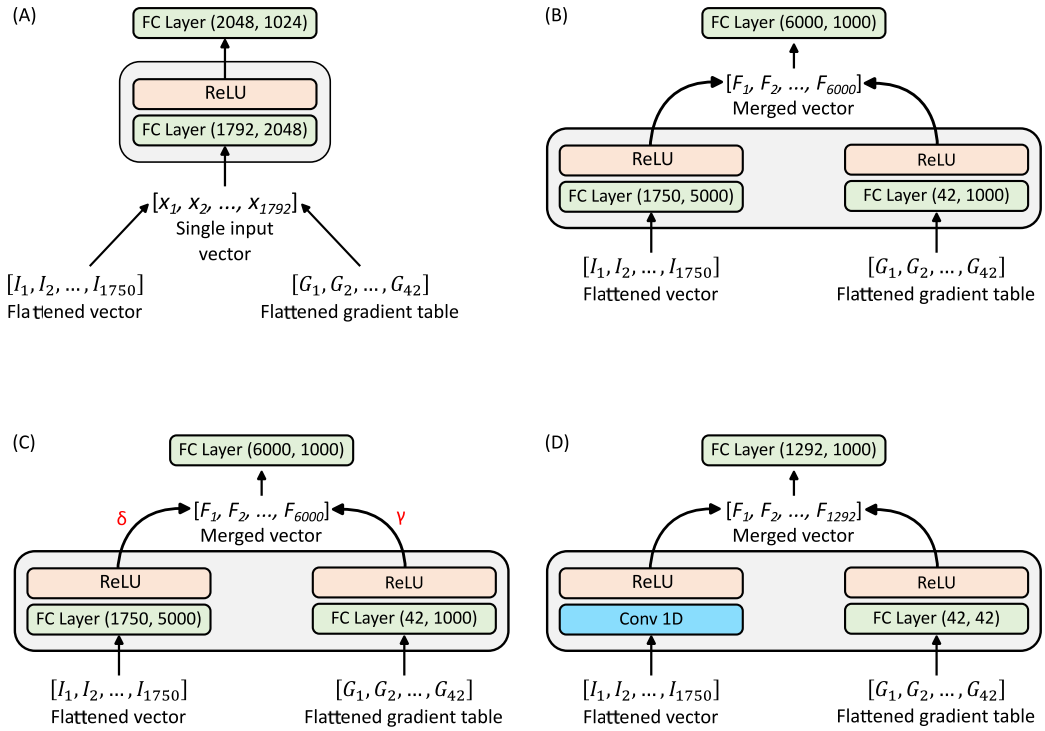

Fig. 3. Array of different model variants: Minimal Model (A), Dual Input Model — DIM (B), Dual Input Model with importance weights — DIM-w (C), and Dual Input Model with convolution layer — DIM-conv (D); $I_1, I_2, I_3, \ldots$ are elements of B.

However, it adds a step where the resulting tensors from the input stage are multiplied by two scalar values, δ and γ. These two values are trainable parameters of the model. The objective was to enable the model to discern which portion of the input is more crucial for achieving the anticipated prediction, hence the designation of these values as significance weights. A significant discrepancy between the two would indicate a markedly disparate level of input importance. While it is conceivable that the two layers of the input stage may perform analogous to one bigger layer, the introduction of these two scalar values is more straightforward and allows for a certain degree of explainability.

The final model tested was a DIM model with convolution (DIM-conv, Fig. 3D). The layer responsible for processing the flattened DWI signal vector was replaced by a one-dimensional convolution layer with a kernel size of 5, a stride value of 2, and 250 output channels. The output of the 1D convolution layer is a vector with a length of 1250. Consequently, the layer processing gradients table has a considerably smaller output size in comparison to other architectures.

The output layer, in the case of all architectures, generates a tensor $O \in \mathbb{R}^{\Theta\times\Theta\times\Theta}$. Each value represents an individual voxel and describes the probability with which it contains the same neural tract as the central voxel.

4.2. Tracking with a path search algorithm

Fig. 4 presents a neural tracking within a single cube in two dimensions for simplicity. The processing of diffusion-weighted imaging (DWI) data by a neural network yields a tensor $O \in \mathbb{R}^{\Theta\times\Theta\times\Theta}$ of probabilities p (see Fig. 4A). It is assumed a priori that a central voxel s contains a currently elongating neural tract, or a seed point when new tracking begins, and thus the probability for s is 1. Therefore, the result can be interpreted as a weighted directed graph of possible connections between neighboring voxels (Fig. 4B). Each voxel is represented as a node. The weights for the edges incoming to a given vertex are equal to $1 - p$, as given by the neural network output. This approach to data interpretation reduces the problem of determining the position of the neural tract to finding the optimal path between the center of the cube and its edge targets (t_1 and t_2) (Fig. 4C). In this setting, an optimal path represents the most probable trajectory of the neural fiber in three-dimensional space. Given that the edge weight is expressed as $1 - p$, minimizing the cost of the path, in turn, maximizes the probability. The shortest path algorithm, exemplified by the Dijkstra algorithm (Dijkstra, 1959), can be used for that. However, a graph represents voxels of a constant size, reflecting a real tissue volume. When finding a path between the origin and a target point (voxel), one can use a straight-line Euclidean distance d between the two points as a heuristic method to accelerate the computation (Fig. 4C). Therefore, we decided to implement fiber tracking using the A* algorithm (Hart, Nilsson, & Raphael, 1968).

Fig. 5 visualizes the process of streamline elongation across multiple cubes. The algorithm for computing the entire tractogram T as a set of streamlines S is defined as follows.

Step 0: Let c denote the seed point at position $c = [x, y, z]$, Θ the size of the sample cube, τ the threshold for a positive class for a trained HyTract ANN, W the termination distance in voxels from the seed point, and $B \in \mathbb{R}^{\Theta\times\Theta\times\Theta\times L}$ the four-dimensional diffusion data tensor.

Step 1: Define an empty set of temporary streamlines $H = \emptyset$, and an empty set of finished streamlines $J = \emptyset$.

Step 2: Add a 1-element streamline containing seed point c to the set H. At this moment the seed point becomes the end of the currently considered streamline, $c = s^i_{k_i}$.

Step 3: While $H \neq \emptyset$, for each streamline S^i in the set H:

Step 3.0: Remove streamline from the set H and store locally as $S^i = (s^i_1, s^i_2, \ldots, s^i_{k_i})$

Step 3.1: Draw $B \in \mathbb{R}^{\Theta\times\Theta\times\Theta\times L}$ from the DWI measurement Ω so that the center is aligned with the end of the current streamline $s^i_{k_i}$.

Step 3.2: Analyze data with a HyTract ANN to obtain a tensor of probabilities $O \in \mathbb{R}^{\Theta\times\Theta\times\Theta}$.

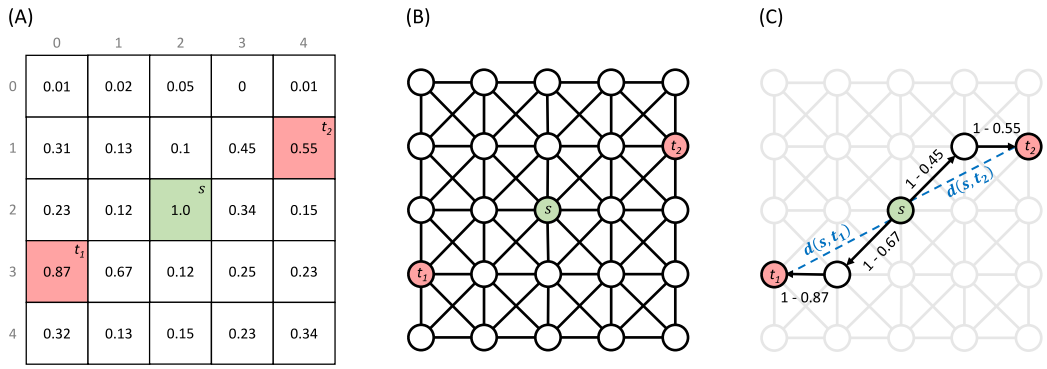

Fig. 4. Graph representation and a heuristic path search within a single cube. (A) ANN output representation in 2D; (B) A graph constructed based on the ANN output; (C) A path search schematic view with heuristic measures d between starting node (s) and target nodes (t_1 and t_2); float numbers associated with edges are their weights.

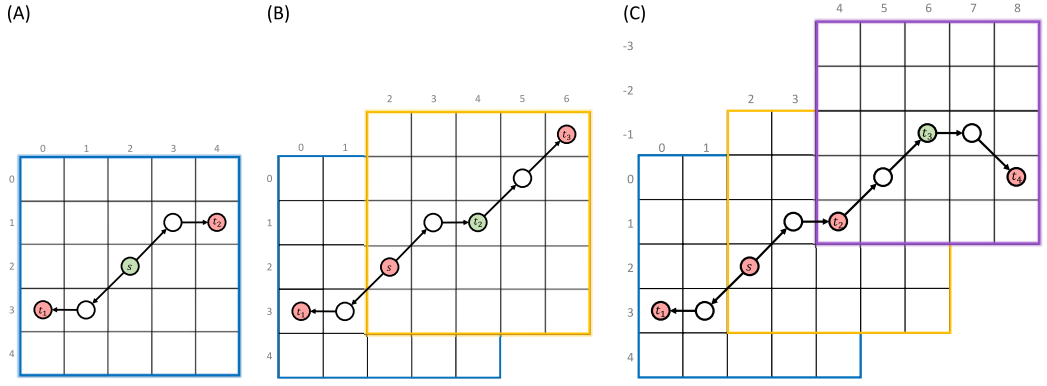

Fig. 5. Elongating streamlines by sampling consecutive cubes from the diffusion data.

Step 3.3: Define set of border (edge) targets $U = (t_1, t_2, \ldots, t_U)$, where $t_l \geq \tau$, $l = 1, \ldots, U$ and $t_l \notin S^i$.

Step 3.4: For all U border targets:

- Compute a path from the cube center to the target using the A* algorithm.
- Elongate streamline S^i by the computed path.
- Check if Euclidean distance $d(s_1^i, s_{k_i}^i) \geq W$.
  - · if yes, save the streamline to finished streamlines set J.
  - · if no, save the streamline to unfinished set H.

To compare the effects of streamline elongation with Dijkstra and A* algorithms we constructed several streamlines originating at the same seed point. Fig. 6 depicts reconstruction computed with Dijkstra algorithm (A) and A* algorithm (B), clearly showing both are the same. Therefore, A* shall be selected over Dijkstra due to better efficiency.

Due to the fact that this method operates on the voxels, a resulting streamline might contain sharp turns, such as those illustrated schematically in Fig. 7. This is not a natural alignment of the neural fibers within the brain. Hence, a smoothing method is required to interpolate the results. For this, we have used a simple moving average (SMA), which is commonly used in financial applications for price chart smoothing (Chou, 1969). This method averages υ points from the streamline $S^i = (s_1^i, s_2^i, \ldots, s_{k_i}^i)$. The mean over last υ voxels s can be calculated as follows:

$$SMA^i = \frac{s^i_{k_i-\upsilon+1}, s^i_{k_i-\upsilon+2} + \cdots + s^i_{k_i}}{\upsilon} = \frac{1}{\upsilon} \sum_{q=k_i-\upsilon+1}^{k_i} s_q^i, \tag{1}$$

We have computed a smoothed result for a set of crafted examples with the window sizes $\upsilon = (3, 5, 7)$ to assess empirically the proper window size. As illustrated in Fig. 7, the larger the window size, the smoother a streamline becomes. However, the anatomic relevance of such smoothing can be questioned when the result deviates significantly from the original tract. Such a situation can be observed in Fig. 7C and D in a U-shaped turn marked with arrows. Hence, a smaller window size of $\upsilon = 3$ should be used, as it is still able to fix artifacts created by favoring diagonal transition between voxels (see regions marked with arrows in Fig. 7B).

5. Preparation of the training dataset

Training machine learning models for tractography imposes a challenge, given there is no ground truth tractograms available. Tractography methods frequently yield a high incidence of false positive results, leading to the generation of spurious tracts. The presence of too many false positive results narrows the usable operating field, making it difficult to plan the surgery.

In this study, we introduce a novel approach to generate training and validation dataset of streamlines using multiple methods selected from the literature. Fig. 8 depicts the process which consists of the following steps:

1. The base tractograms are computed with methods selected from the literature for the same set of seed points (Fig. 8A).
2. One of the base tractograms, typically the one containing the highest number of streamlines, is picked as a reference (Fig. 8A, blue color).
3. Each streamline in a given reference is compared in a pairwise manner with the counterparts in other base tractograms (Fig. 8A, red and green colors).
4. A streamline is added to the dataset (Fig. 8B) if there are counterparts meeting certain criteria:

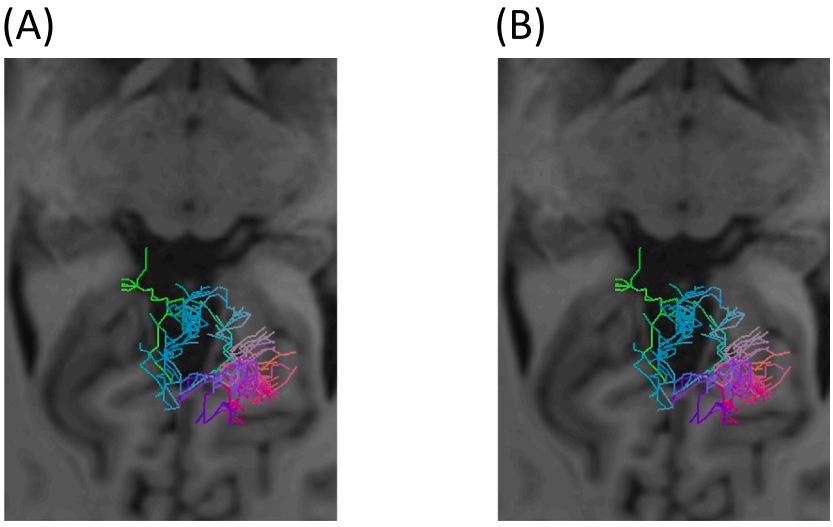

Fig. 6. Comparison of streamlines reconstructed with Dijkstra (A) and A* (B) algorithms.

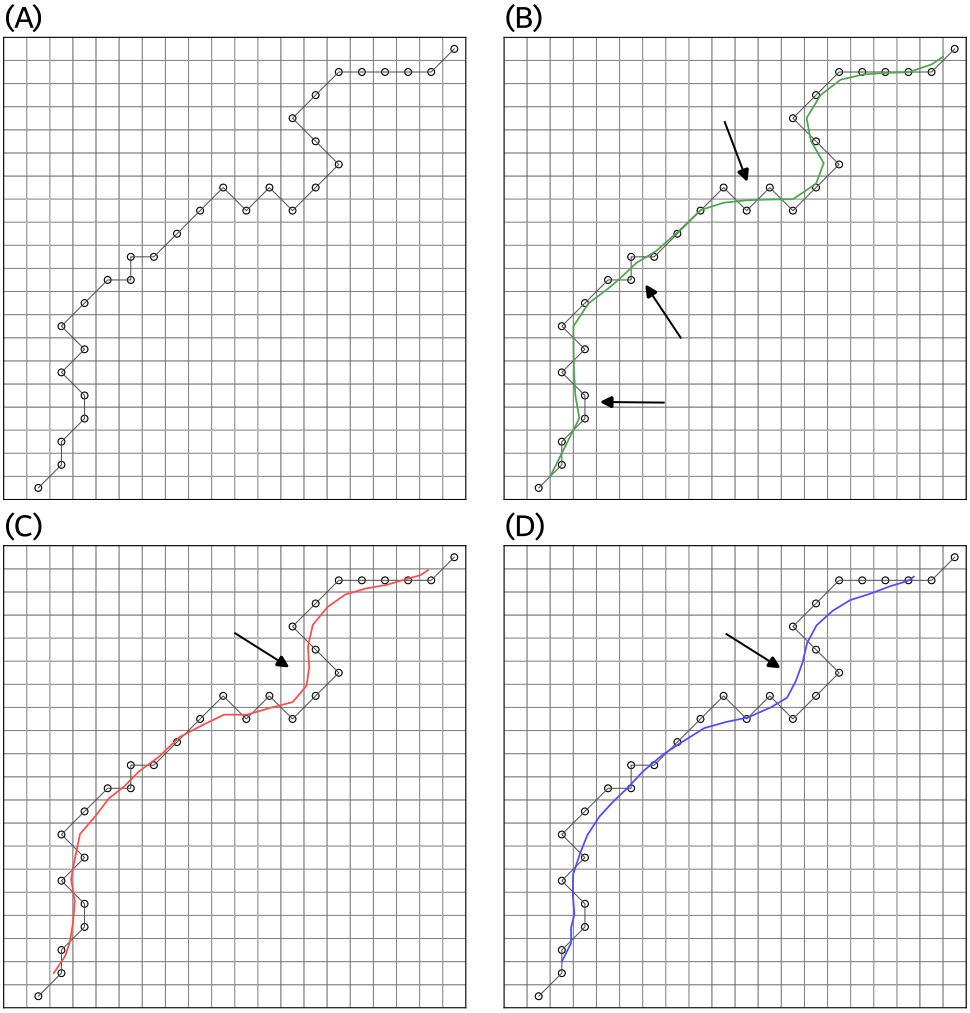

Fig. 7. Smoothing calculated tracts with SMA for $\upsilon = (3, 5, 7)$.

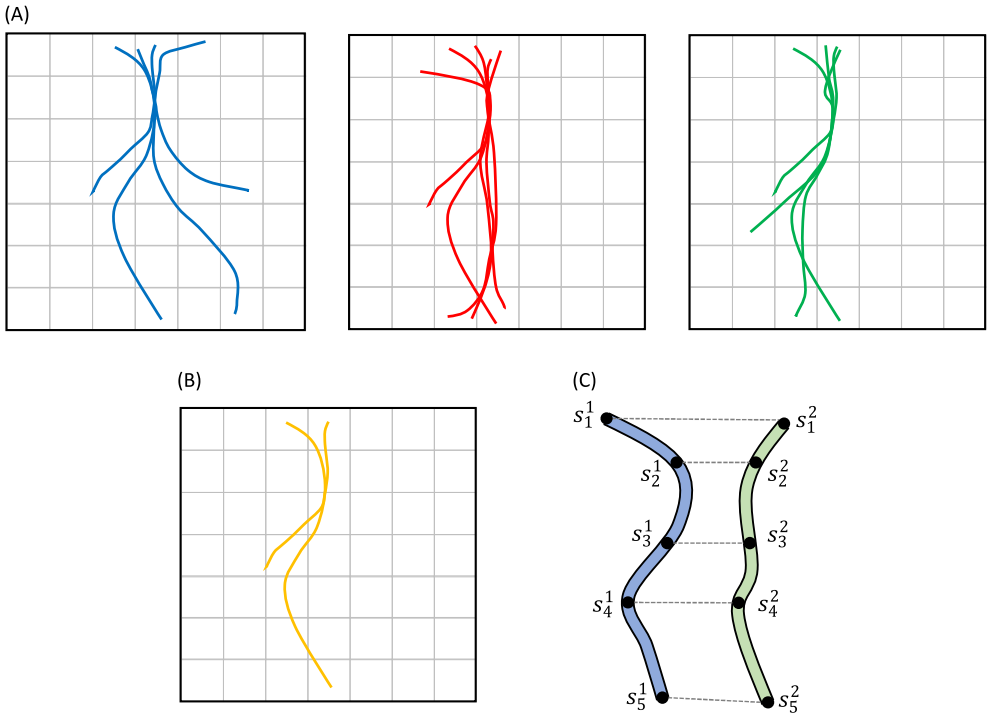

Fig. 8. The generation of the training and validation dataset.

- the length of the shorter one is at least $\beta\%$ of the longer one.
- the similarity measure between the two streamlines is below a certain threshold (assuming measures where identical streamlines will give value of 0).

Such an approach allows to filter out false positive streamlines from the final dataset, which comprise only those tracts that have been confirmed by other methods.

Fig. 8C depicts the manner in which two streamlines can be compared. Each streamline can be considered as a set of points in three-dimensional space, connected in a particular order. We propose to compute the similarity between the two streamlines as a Mean Euclidean Distance (MED) between the respective points:

$$MED = \frac{1}{m}\sum_{j=1}^{m}\sqrt{(x_j^1 - x_j^2)^2 + (y_j^1 - y_j^2)^2 + (z_j^1 - z_j^2)^2}, \quad (2)$$

where m represents the length of the shorter streamline, and $[x_j^i, y_j^i, z_j^i]$ are the coordinates of the jth voxel of the ith streamline. For each of the reference streamline, we selected the streamlines with the lowest MED from the other methods as their closest counterparts. In the case when the length of the two considered streamlines differs, the MED is calculated for the entire length of the shorter streamline.

The resulting tractogram represents the average of the three base methods used. Hence, we name it a consensus tractogram. There are certain advantages to using such an approach. A tractogram computed with a single method often suffers from inconsistencies due to stochastic variability, incomplete fiber reconstruction, and high incidence of false positive or false negative connections. The fibers of the consensus tractogram are those that have been confirmed by other methods, hence limiting the probability of a high incidence of false positive tracts. By adjusting the strategy of comparing different tractograms with each other, one can undoubtedly improve tractography output and adapt based on the domain knowledge. We identify this approach as a novel research area that we plan to investigate further to propose comprehensive methods and metrics for comparing single tracts with each other.

6. Implementation and training

6.1. Dataset creation

To compute tractograms for the generation of the training and validation dataset we used MRI data from the Human Connectome Project (HCP) database (https://ida.loni.usc.edu/login.jsp). HCP is the result of efforts of co-investigators from the University of Southern California, Martinos Center for Biomedical Imaging at Massachusetts General Hospital (MGH), Washington University, and the University of Minnesota (Feinberg et al., 2010; Moeller et al., 2010; Setsompop et al., 2012; Essen et al., 2012; Xu et al., 2012).

For the training and validation data sets, we randomly selected five individuals (subjects): mgh_1007, mgh_1010, mgh_1016, mgh_1019, and mgh_1031. For each of the five randomly selected subjects, we generated streamlines for tracts originating at the gray-white matter interface of Broca's area. The complete process of creating labels is illustrated in Fig. 9. As the initial step, a T1-weighted image was coregistered with an initially preprocessed DWI image to ensure uniform resolution and space. To achieve this, a gradient-free image from the DWI measurement was extracted using the dwiextract tool from the MRtrix3 package (Tournier et al., 2019). The T1-weighted image was then registered to extracted gradient-free image using Linear Image Registration Tool (FLIRT) (Greve & Fischl, 2009; Jenkinson, Bannister, Brady, & Smith, 2002; Jenkinson & Smith, 2001) from FSL software package (Jenkinson, Beckmann, Behrens, Woolrich, & Smith, 2012; Smith et al., 2004; Woolrich et al., 2009), with six degrees of freedom for transformation. In order to prepare a set of seed points for tractography from the gray-white matter interface of the Broca area, three masks were created using a coregistered T1 image. These were a white matter mask (WM mask), a gray-white matter interface mask (GMWMI mask), and a functional mask for the Broca area.

The white matter mask was used to restrict the scope of tractography algorithms computation. This was achieved by computing a five-tissue-type (5TT) segmented tissue image from the T1 image using the 5ttgen tool (Smith, Tournier, Calamante, & Connelly, 2012) from the MRtrix3 package. A skull was removed and the brain was extracted

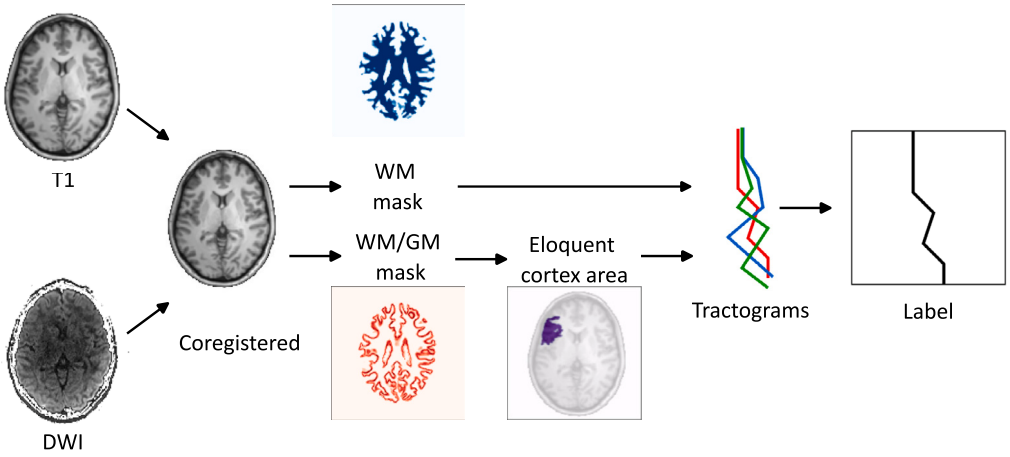

Fig. 9. Training label preparation pipeline.

using the BET2 tool (Jenkinson, Pechaud, & Smith, 2005; Smith, 2002) from the FSL package. This process allows for the straightforward extraction of a white matter mask (WM mask) from the 5TT image. A second mask, a gray-white matter interface mask (GMWMI mask), was obtained from the 5TT image using a dedicated tool, 5tt2gmwmi (Smith et al., 2012), which is also from the MRtrix3 package.

The primary objective was to perform tractography of fibers originating in the Broca area. To accomplish that a set of seed points for tractography algorithms was created to cover the gray-white matter interface of the region of interest. A mask for the entire Broca region in MNI152 space (Fonov et al., 2011; Fonov, Evans, McKinstry, Almli, & Collins, 2009) was retrieved from the Juelich histological atlas (Amunts et al., 1999) using FSLeyes (McCarthy, 2023) of the FSL package. The FLIRT and FNIRT (Andersson, Jenkinson, & Smith, 2010) tools from FSL were employed to compute transformation matrices, which were used to transform images from the MNI152 space to the subject space. The GMWMI mask (from a 5TT image) was overlaid with a functional mask, providing a set of seed points for tracking algorithms.

Three methods were used to compute base tractograms. The EuDX algorithm was used with the Constant Solid Angle (CSA) model (Garyfallidis, 2012) (Fig. 10A), Closest Peak Direction Getter (CPDG) with Constrained Spherical Deconvolution (CSD) model (Garyfallidis et al., 2014) (Fig. 10C), and Deterministic Maximum Direction Getter (DMDG) with CSD model (Garyfallidis et al., 2014) (Fig. 10C). The EuDX algorithm yielded the highest count of streamlines, thus it was selected as a reference. To create a set of streamlines for training and validation, we decided to set $\beta = 80\%$, and to consider three MED thresholds: 1 voxel (Fig. 10D), 2 voxels (Fig. 10E), and 3 voxels (Fig. 10F). The dataset with the most restrictive MED value of 1 did not contain any tracts that extended beyond the Broca area. In contrast, the tractogram with a MED value of 2 did contain such tracts, but in a limited number. Therefore, we decided to use the dataset with streamlines picked with a MED value of three or less. The final training and evaluation dataset consists of 78,178 streamlines. The dataset has been divided into training and evaluation with a ratio of 8:2, with 62,544 and 15,634 streamlines respectively. The division was made for each subject separately to ensure each is equally represented in training and evaluation. An individual label is generated for each streamline in the consensus tractogram independently. This is a three-dimensional binary tensor of the same size as the entire DWI scan. Voxel value is set to 1 if a streamline overlaps it. All remaining voxels are assigned a value of 0.

6.2. Implementation

The method was implemented using Python programming language. Neural networks were implemented using PyTorch (Paszke et al., 2019) and Numpy (Harris et al., 2020). The latter was used to implement a path search algorithm as well. Charts for the figures were plotted using Matplotlib (Hunter, 2007).

Neural networks were trained using various parameters of a learning rate and weight decay. Three different optimizers for backpropagation were used: Stochastic Gradient Descent (SGD) (Robbins, 2007), Adam (Kingma & Ba, 2017), and a Sharpness-Aware Minimization (SAM) (Foret, Kleiner, Mobahi, & Neyshabur, 2021; Kwon, Kim, Park, & Choi, 2021). As a loss function, a Binary cross entropy loss was used (Goodfellow, Bengio, & Courville, 2016).

6.3. Training and validation

We conducted a series of experiments to develop the best ANN model to be used in the HyTract method. We compared the performance of the HyTract for:

(a) various ANN architectures and learning parameters,
(b) different optimization algorithms,
(c) various sample sizes.

The following subsections define respective scenarios and describe their results.

6.3.1. Various ANN architectures and learning parameters

This experiment was designed to identify the optimal architecture among those proposed in the method overview. A set of learning parameters was selected to ensure reliable comparison of results. Each of the presented architectures was trained for 100 epochs with learning rates of 1e−3, 1e−4, and 1e−5. Even with such a short training period, we observed that the loss function decline was satisfactory, and that the ROC AUC reached values close to 1 for the training dataset. Therefore, it was deemed rational to use such a constraint to compare different proposed architectures and learning parameters in a reasonable time period. The training sessions were run using the Adam optimizer and Binary Cross Entropy loss function (Goodfellow et al., 2016).

The two models that exhibited the highest ROC AUC on the evaluation dataset were DIM and DIM-w (Table 1). Fig. 11 illustrates a typical training pattern observed for the DIM-w model. During the initial 100 epochs, the loss function value exhibited a consistent decline (Fig. 11A), with no indication of over-training. The ROC AUC (Fig. 11B) demonstrates a gradual increase, reaching values approaching 1 for the training dataset. The optimal learning rate was determined to be 1e−4. The loss function on the validation dataset reached a value of 0.1028 for DIM and 0.1038 for DIM-w models. The ROC AUC value was 0.9587 for DIM and 0.9578 for DIM-w model. In the case of the latter, the significance weights reached values $\gamma = 0.0622$, associated

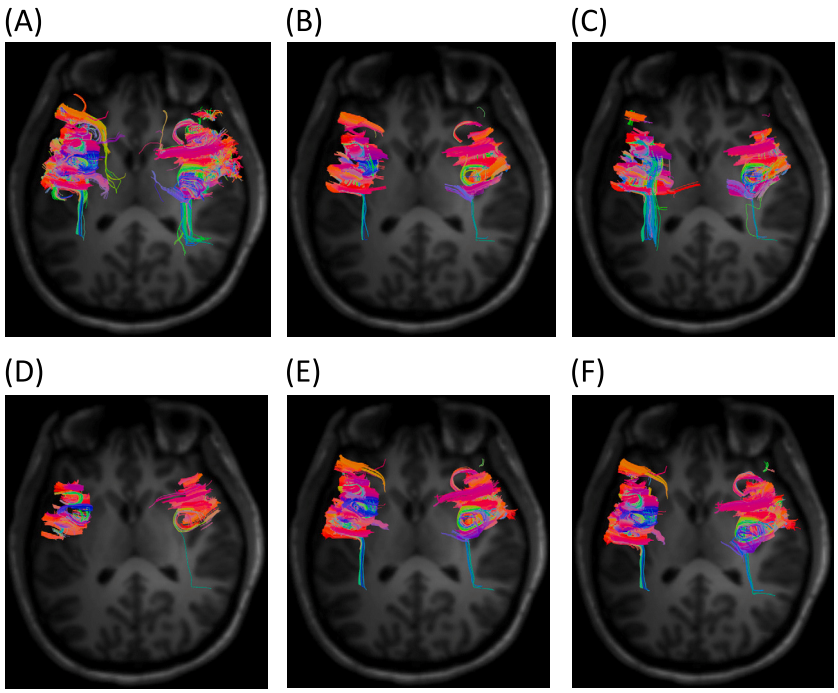

Fig. 10. Streamline datasets with different MED threshold values. Upper row represents basal tractograms created with EuDX (A), CPDG (B), and DMDG (C) methods. The lower row represents meta-tractograms derived from previously mentioned methods, at the MED thresholds of 1 voxel (D), 2 voxels (E), or 3 voxels (F).

Table 1
ANN models performance with different architectures (training and validation phases). MM — Minimal Model; DIM — Dual Input Model; DIM-w — Dual Input Model with weights; DIM-conv — Dual Input Model with convolution.

Architecture	Learning rate	Min Loss		Max ROC AUC	
		Train	Val	Train	Val
MM	1e−3	0.118	0.1248	0.9378	0.928
	1e−4	0.0984	0.1082	0.9628	0.9531
	1e−5	0.1069	0.1093	0.9534	0.9505
DIM	1e−3	0.1046	0.1103	0.9563	0.9496
	1e−4	0.0925	0.1028	0.9685	0.9587
	1e−5	0.1046	0.1068	0.9562	0.9536
DIM-w	1e−3	0.1105	0.1159	0.9488	0.942
	1e−4	0.0922	0.1038	0.9687	0.9578
	1e−5	0.1028	0.1056	0.9581	0.9551
DIM-conv	1e−3	0.1013	0.1104	0.960	0.950
	1e−4	0.0941	0.1062	0.967	0.9552
	1e−5	0.1106	0.112	0.9484	0.9467

with the gradient table, and $\delta = 4.2595$ associated with the diffusion data (Fig. 3). The DIM-w achieved performance that was very similar to that of the DIM model. However, it includes the significance weights, which are an interesting addition in terms of explainability. Therefore, we decided to use the DIM-w model in all subsequent experiments.

The efficacy of various values of the weight decay (Krogh & Hertz, 1991) was evaluated on a DIM-w model to ascertain whether it would enhance the model's performance. Fig. 12 depicts the outcomes of three experiments with weight decay values of 1e−2, 1e−3, and 1e−4. The plots for the learning loss and ROC AUC values clearly indicate that the use of weight decay did not improve the model performance. The learning loss did not decrease for any of the tested weight decay values. Despite the ROC AUC increasing during training for each experiment, it remained constant for the validation dataset, indicating no improvement in terms of generalization. Therefore, it was determined that the final model would not be trained using weight decay.

6.3.2. Different optimization algorithms

Although the Adam optimizer is the most widely used, other algorithms have been demonstrated to perform and generalize better in certain cases (Wilson, Roelofs, Stern, Srebro, & Recht, 2017). In addition to Adam, two other optimization strategies were tested on the DIM-w model: a classical Stochastic Gradient Descent (SGD) (Robbins, 2007) and a Sharpness-Aware Minimization (SAM) (Foret et al., 2021; Kwon et al., 2021). The SAM method is a technique that simultaneously minimizes loss value and sharpness. Therefore, it requires an optimization algorithm to operate on. The experiment were run with Adam, SGD, and SAM with either SGD or Adam serving as the optimization algorithm's foundation. Fig. 13 summarizes the training results in terms of the learning loss and ROC AUC. For the SGD optimizer and SAM with SGD as the backbone, the learning loss decreased in the first few epochs and remained constant for the remainder of the training. The ROC AUC for these two optimizers reached levels below 0.85, which is considerably less than for other optimizers. The plots exhibited a similar trend for both the training and validation phases. In the case of Adam and SAM with Adam backbone, consistent decline in learning loss can be observed throughout the entirety of the training process. The values of ROC AUC are comparable and reach levels above 0.95, which are typical for the Adam optimizer, as evidenced by the experiments that elucidated the optimal architecture. The use of SAM optimizer with Adam backbone did not result in superior outcomes. This indicates that the pure Adam optimizer gives the best performance.

6.3.3. Various sample sizes

One of the parameters of a neural network that can profoundly affect the path search stage is the size of the sample analyzed in a single step. As the cube size increases, the amount of data processed by the network increases, the number of parameters grows (see Table 2), and the granularity of the search changes. The DIM-w neural network was trained with three cube sizes: $5 \times 5 \times 5$ with close to 15 million parameters, $7 \times 7 \times 7$ with over 30 million parameters, and $9 \times 9 \times 9$ with almost 58 million parameters. A cube of dimensions $3 \times 3 \times 3$ was not considered, as in such a case, the voxels on the border are direct neighbors of a central voxel. Consequently, there is a paucity of space for the path search algorithm to operate effectively.

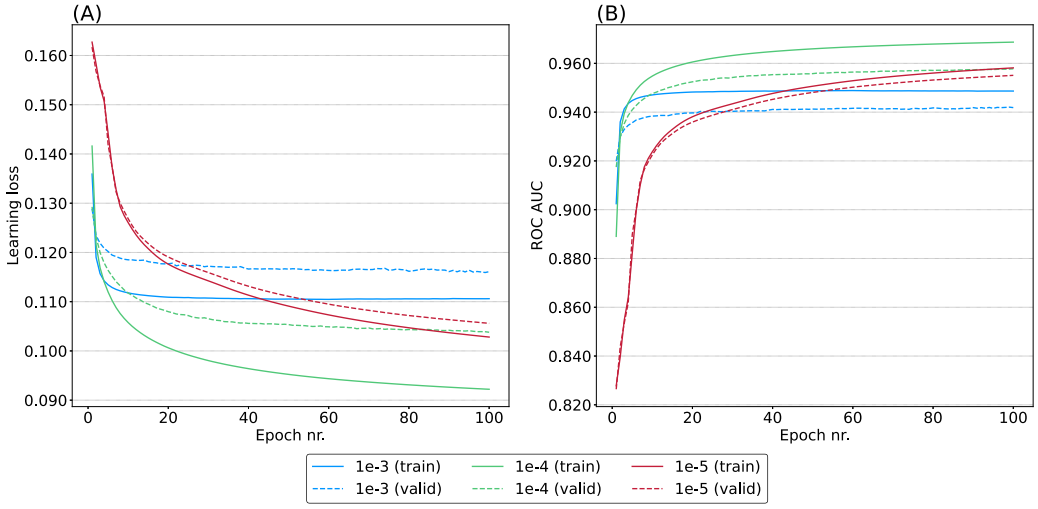

Fig. 11. The results of the DIM-w model training. Panes depict graphs of a loss function (A) and ROC AUC performance measure (B). Solid lines represent the training phase, while dashed lines evaluation. Different colors represent training with respective learning rates.

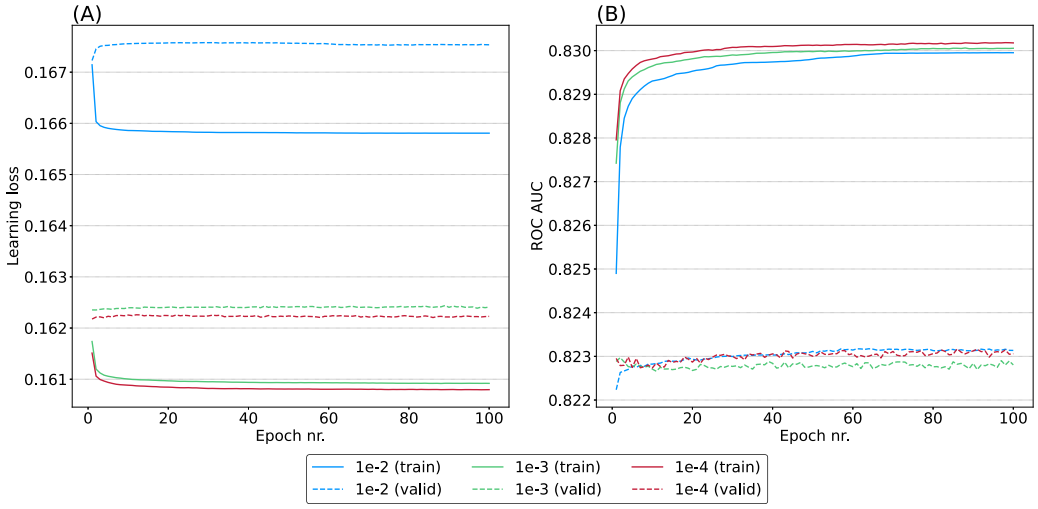

Fig. 12. The results of the DIM-w model training using various weight decay values.

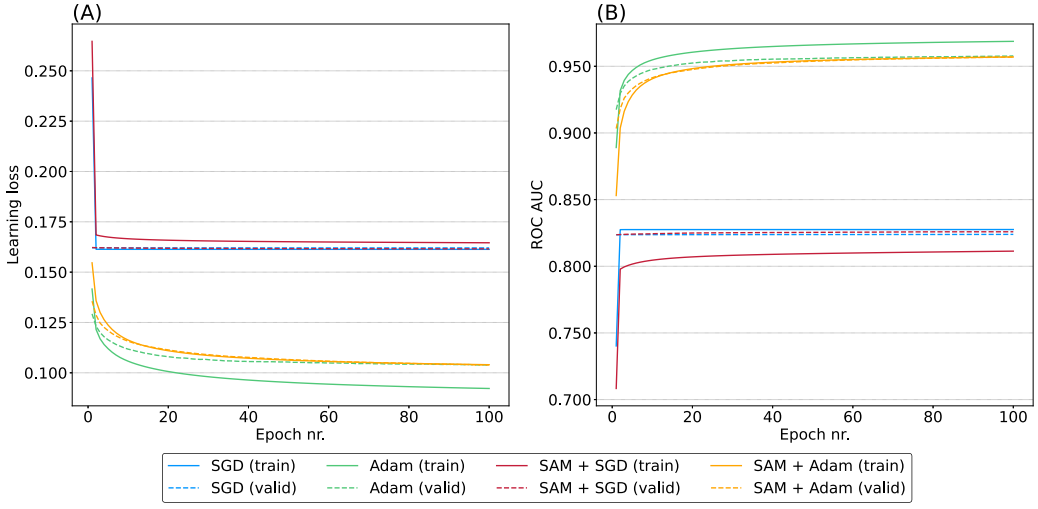

Fig. 13. The results of the DIM-w model training using various optimization algorithms.

Table 2
Effect of cube size on the number of trainable model parameters in a DIM model architecture.

Cube size	Number of parameters
5 × 5 × 5	14 938 127
7 × 7 × 7	30 416 345
9 × 9 × 9	57 822 731

Table 3
Loss and ROC AUC values for training DIM-w model with various cube sizes.

Cube size	Min loss		Max ROC AUC	
	Train	Val	Train	Val
5 × 5 × 5	0.0865	0.1012	0.9734	0.9610
7 × 7 × 7	0.0487	0.0579	0.9824	0.9717
9 × 9 × 9	0.0307	0.0369	0.9875	0.9788

All three variants were trained on the same dataset, with the same parameters of learning rate 1e−4, and weight decay set to 0. Values for a loss function and ROC AUC are summarized in a Table 3. The model variants with a cube size of 7 and 9 significantly outperform the one with a cube size of 5. The model with a cube size of 7 achieved an ROC AUC of 0.9714 on a validation dataset after 100 training epochs. The model with a cube size of 9 reached an even higher ROC AUC value on the same dataset, at 0.9787.

One potential explanation for this phenomenon is the number of parameters (see Table 2). The model for a cube size of 7 is approximately twice as large as the model for a cube size of 5. The model for a cube size of 9 is even larger, with a total of almost 58 million parameters. Additionally, the view is much broader in larger cubes, allowing us to verify whether a branching fiber has a continuation and is a true fiber, or if the branching is just merely a data error.

7. Testing results

DIM-w model was trained and picked as the optimal architecture to compute probabilities for the streamline reconstruction with the heuristic A* algorithms. In this section we describe experiments aimed at the computation of the tractogram originating in the primary visual cortex. These experiments were performed on the data from a subject not present in the training and validation dataset.

7.1. Testing dataset

The following experiments were carried out on the testing dataset, which was created to test for subject and region-related bias. Another individual (subject), mgh_1027, was randomly selected from the HCP dataset and three tractograms were computed using the same approach as described in the Section 6.1. However, in this case, the V1 primary visual cortex (Amunts, Malikovic, Mohlberg, Schormann, & Zilles, 2000) was selected as the functional area. Moreover, we did not filter streamlines with the MED similarity measure, as our intention was to directly compare HyTract tractograms with base tractograms computed using EuDX, DMDG, and CPDG methods, as presented in Fig. 14.

7.2. Tract reconstruction for V1 primary cortex for the test subject

DIM-w models for cube sizes of 5, 7, and 9 were used to reconstruct neural tracts originating in the V1 primary cortex. In the streamline elongation phase a set of $\tau = (0.4, 0.5, 0.6, 0.7, 0.8, 0.9)$ values was picked for marking target vertices on the sample border. Multiple values of τ as the method is not limited to a single value. Manipulating this value will result in streamlines of varying confidence, allowing to construct a tractogram that best suit a specific need. The stopping criterion was set to $W = 70$ voxels to avoid reconstructing very long tracts. All other parameters were held constant. Streamlines with a length of less than 15 voxels were deemed unsuitable, as such short tracts are typically spurious. Table 4 summarizes these experiments. HyTract method with a cube size of 5 computed streamlines longer than 15 voxels only for $\tau = 0.4$. Tractograms computed with a cube size of 7 and 9 contain a considerable number of streamlines exceeding 15 voxels, with some exceeding 100. Given that the stopping criterion distance was measured in a straight line between the origin (s_1^i) and the current end of the streamline ($s_{k_n}^i$), the presence of such long streamlines is not unexpected. When a more restrictive threshold value is used, the number and mean length decrease as expected. As the size of a single sample is increased, the number of computed streamlines and their length also increase. This finding is consistent with previous conclusions, which indicated that larger cube sizes yielded superior model performance due to the broader interpretation of the data. Furthermore, the path between the cube center and the border is longer, allowing for the passage through the voxels of lower values, which might otherwise have been excluded.

Table 4
Statistics of streamlines computed with a HyTract method for various cube sizes and border target thresholds.

Cube size	Threshold	# streamlines	Streamline length	
			Mean	Max
5 × 5 × 5	0.4	4	17	18
7 × 7 × 7	0.4	4848	24.80	73
	0.5	1190	22.53	46
	0.6	403	19.86	33
	0.7	67	18.46	26
	0.8	18	16.94	21
9 × 9 × 9	0.4	12 899	32.79	105
	0.5	6459	24.94	51
	0.6	3373	24.21	92
	0.7	889	20.69	48
	0.8	449	18.73	40
	0.9	296	18.90	36

A visual evaluation of the streamlines reveals that the HyTract method is capable of accurately computing tracts originating within the primary visual cortex. In addition to a short-range tracts that are restricted to the V1 area alone, three long-range association fiber bundles are visible in Fig. 15B, which are expected to be present anatomically (Vanderach & Gould, 2016). One of these tracts moves superior to the corpus callosum and rostral towards the frontal lobe. The second tract reaches towards the thalamus, while the third towards the temporal lobe.

7.3. Comparison with base tractograms

All HyTract tractograms were compared to the tractograms computed by the reference methods (EuDX, CPDG and DMDG) using mean Euclidean distance. This was achieved by identifying the closest fiber equivalent for each HyTract streamline in the reference methods. The results of this comparison are presented in Fig. 16, where mean, minimal and maximal MED values registered for the closest counterparts of a HyTract streamlines in reference methods are given. The color gradient represents low values in bright and high values in dark color. Vertical axis denote various threshold values τ for a given cube size, and horizontal axis represent reference methods.

The HyTract streamlines exhibited the closest proximity to the EuDX tractogram, with a mean MED below 10 voxels for cube size of 7 with threshold values of 0.4, 0.6, and 0.8. Additionally, the same was observed for cube size 9 with threshold values of 0.8 and 0.9. These tractograms are presented in three anatomical planes in Fig. 15. It should be noted that tractograms with a cube size of 7 and a threshold of 0.8, as well as with a cube size of 9 and a threshold of 0.9, have been omitted from the figure due to the relatively small number of streamlines. Comparison to CPDG and DMDG methods yielded lower

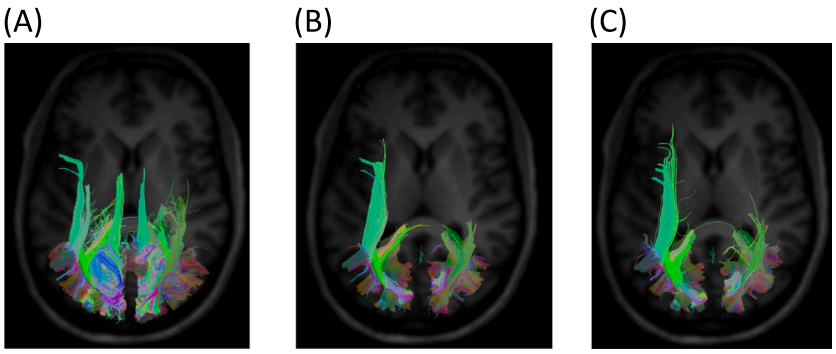

Fig. 14. Tractograms in the test set computed with EuDX (A), CPDG (B), and DMDG (C) methods.

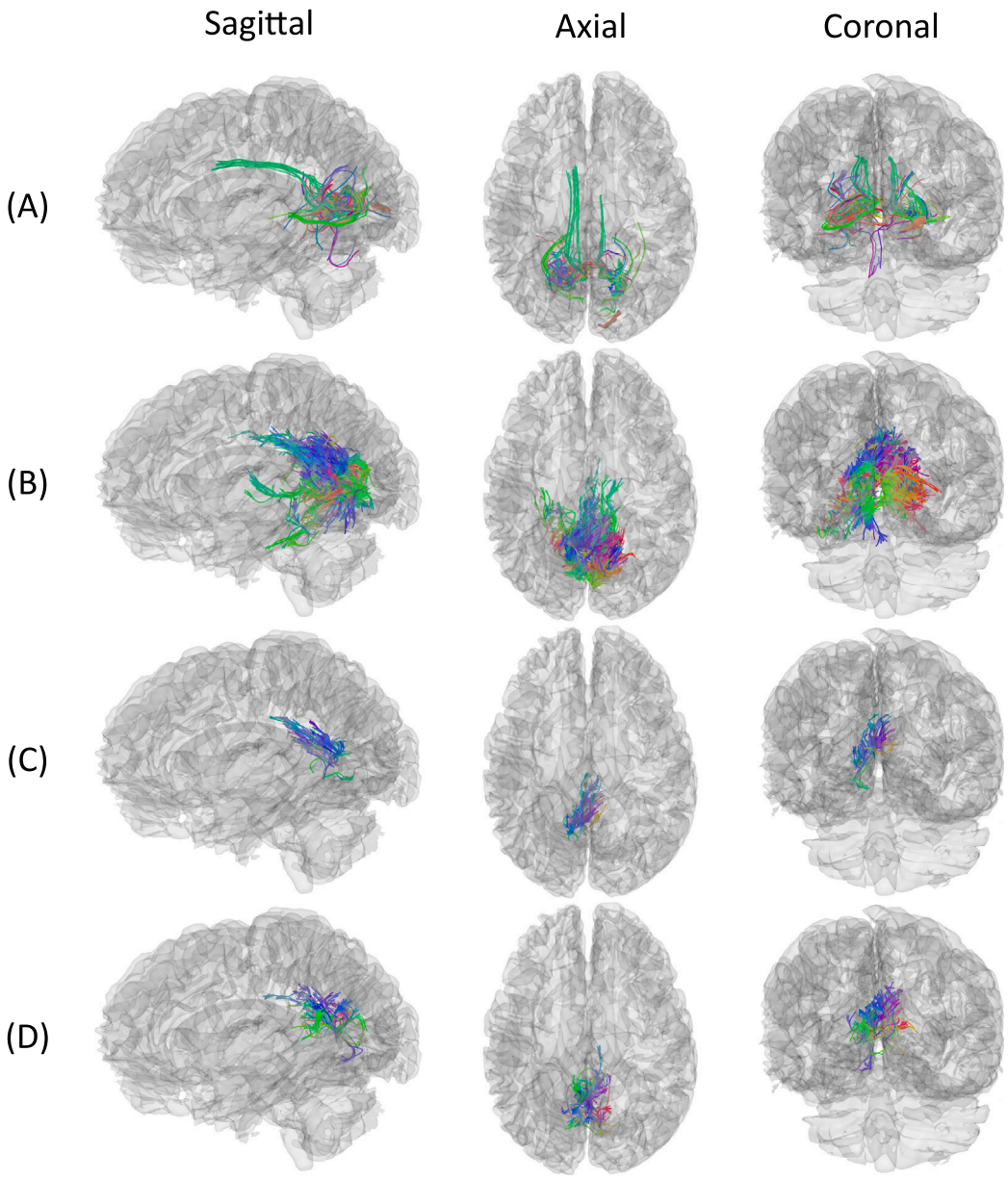

Fig. 15. Tractograms originating in the primary visual cortex (V1) computed with EuDX reference method (A), and HyTract method with cube size 7 and threshold 0.4 (B), cube size 7 and threshold 0.6 (C), cube size 9 and threshold 0.8 (D).

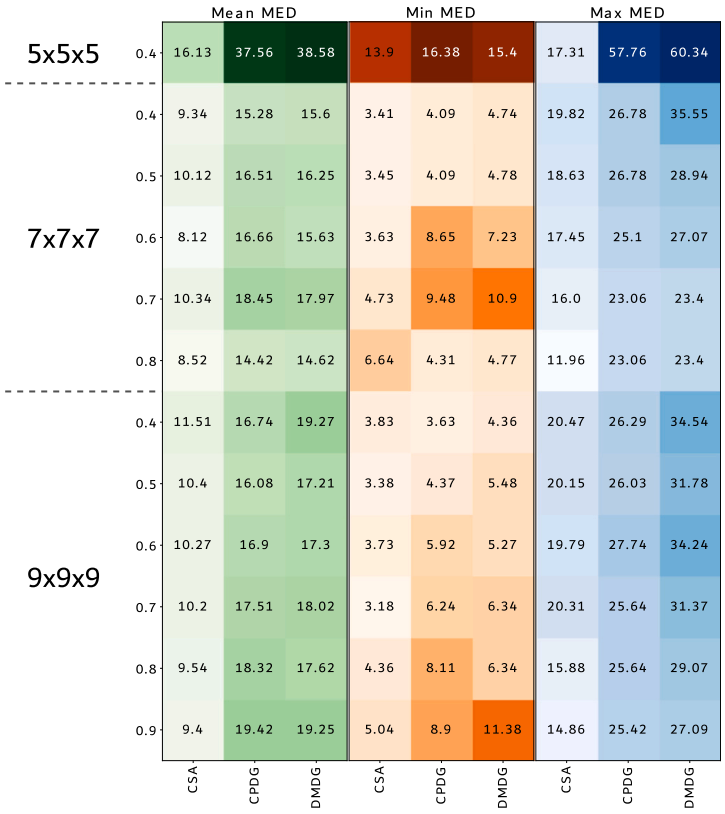

Fig. 16. Heatmap presenting comparison between HyTract tractograms with diverse cube size and threshold values, and three reference methods.

level of similarity with mean MED value above 15. The rationale for this discrepancy is that the EuDX tractogram was selected as a reference for the construction of consensus tractograms. Consequently, the HyTract tractograms will exhibit the highest degree of similarity to the base tractogram computed with this method.

8. Summary and discussion

In this paper we introduce a new tractography technique exploiting the advantages of the machine learning techniques. Due to its hybrid nature we name it HyTract–Hybrid Tractography. The method combines artificial neural network and the A* path search algorithm. The purpose of the neural network is to analyze the diffusion data and generate a graph of possible connections between voxels, representing structural connections within the brain. This reduces the problem of computing neural tracts to finding optimal paths in the graph. The results of experiments reported in this paper confirm the efficacy of the proposed approach.

The neural network models tested for this method were trained on the data from five subjects from the International Human Connectome Project (HCP) initiative. Even though the number of subjects is relatively small, there were more than 78,000 streamlines to train and evaluate on. the ANN analyzes data in small samples, with a single scan providing hundreds of thousands of cubes to train on.

In this paper, we propose a novel method for the generation of training and validation datasets by computing consensus tractograms. This approach leverages the information from the tractograms computed with multiple methods. By selecting one of them as the reference and comparing its streamlines with others with a proposed similarity measure, we are able to construct a set of training and validation streamlines with less false positive tracts. As the similarity measure, we employed Euclidean distance, where the mean distance is computed between two tracts. Despite the fact that this metric may not be the optimal method for comparing tractograms, to the best of our knowledge, there is no other method for comparing individual tracts with each other. Mean Euclidean Distance (MED) provides the opportunity to quantify eventual displacement, shifts of tracts in space, or local deviations, similarly to the RMSD method used in protein design (Li, 2013). In subsequent studies, we aim to develop the concept of consensus tractograms further to investigate suitable similarity metrics for comparing tracts, taking into account anatomical relevance.

Experimental results corroborate this conclusion and demonstrate that the optimal architecture is a Dual Input Model with and without weights (DIM-w and DIM). The DIM-w model may be a more suitable choice given the importance weights, which provide additional explainability. The results with various sample sizes suggest that the ANN can better analyze the diffusion signal when the size is greater. At the same time, the number of samples to analyze decreases as more workload is shifted towards the path search part. In light of these findings, we sough to ascertain whether the utilization of an alternative optimization algorithm, distinct from the gold standard Adam, would result in enhanced outcomes. However, experiments employing SGD and SAM (with both Adam and SGD backbones) demonstrated inferior performance of the model.

The ANN's simple architecture requires significantly less computational power, allowing it to run efficiently on standard hardware without the need for high-end GPUs. This reduces energy consumption, operational costs, and overall carbon footprint, making it more sustainable and environmentally friendly. Additionally, these lightweight models can be effectively trained with sparse amounts of data, making them well-suited for applications where large, labeled datasets are limited or difficult to obtain. Using a training and validation dataset of streamlines filtered with comparison to other methods, limits a number of false positive results, thereby limiting the number of spurious tracts. Future work is necessary to assess whether similarity measures other than the mean Euclidean distance can be employed to better reflect the similarity between tracts, including anatomical relevance. This subject

Table 5
Notation and abbreviations.

Notation	Description
T	Tractogram defined as a set of streamlines.
S^i	ith streamline in a tractogram
s^i_j	jth point in an ith streamline
n	Total count of streamlines in a tractogram
k_i	Total count of points in an ith streamline
$\Omega \in \mathbb{R}^{d_x \times d_y \times d_z \times L}$	Recording of the whole brain volume
$B \in \mathbb{R}^{\Theta \times \Theta \times \Theta \times L}$	Cuboid chank with size Θ
$G \in \mathbb{R}^{3 \times L}$	Gradient table from the DWI experiment
L	Number of acquisitions per DWI experiment with different gradients
$O \in \mathbb{R}^{\Theta \times \Theta \times \Theta}$	Three-dimensional tensor, output of the ANN model
p^i_j	Probability value for the jth voxel of ith streamline
τ	Threshold for picking border targets at the edge of the cube
t_i	Border targets at the edge of the cube
W	Stopping criterion (termination threshold) in voxels
β	Length threshold for comparison between a streamline pair
d	Euclidean distance measure
H, J	Working sets for storing streamlines during the tract reconstruction
υ	The size of the window in Simple Moving Average
CPDG	Closes Peak Direction Getter
CSA	Constant Solid Angle model
CSD	Constrained Spherical Deconvolution
DIM	Dual Input Model
DMDG	Deterministic Maximum Direction Getter
DWI	Diffusion-weighted Imaging
MED	Mean Euclidean Distance
MNI152	Reference space for MRI volume registration
MRI	Magnetic Resonance Imaging
SAM	Sharpness-Aware Minimization
SGD	Stochastic Gradient Descent
SMA	Simple Moving Average
WM	White Matter
WMGMI	White Matter Gray Matter Interface

is of interest to us and represents a research topic that is currently being investigated in depth.

The fiber reconstruction process is undertaken utilizing the A* algorithm, which is an extension of the traditional Dijkstra algorithm. This approach enables the utilization of the Euclidean distance as a heuristic measure, thereby enhancing the efficiency of the reconstruction process. It is noteworthy that the reconstruction of a path can be undertaken with any cube size. However, it should be noted that the A* algorithm is a heuristic approach; therefore, the use of overly large cube sizes may result in a reduction in the efficiency of the method. Consequently, it is recommended to employ cube sizes that do not exceed 9, as experiments with these sizes have yielded satisfactory outcomes.

It should be pointed out that this method does not require tedious preprocessing steps, as the neural network is capable of learning to handle data inadequacies. Furthermore, this is not a black box model, as tractograms are computed with an explanation regarding the underlying data. The ANN provides a tensor of the likelihoods describing the probability of a given voxel containing a neural tract in a given context. This can be visualized as a graph of possible structural connections. Potential users – such as radiologists or neurosurgeons – will be provided with both a graph and computed tractograms, which will offer valuable insight into the rationale behind reconstructing particular streamlines. Experiments with neural tracts originating from the V1 primary visual cortex, employing both phases of the method, indicate that HyTract is capable of precise reconstruction of the desired tracts. This makes it a convenient tool that can be incorporated into the preoperative pipeline for neurosurgery as a decision support system.

The subsequent stage of this project aims to implement the HyTract method in a clinical setting, with the objective of validating its practical applicability. This implementation will serve as an introduction to the forthcoming clinical trials. The implementation is scheduled to take place in the Department of Neurosurgery at the National Oncology Center in Warsaw, where we have ongoing collaborations with neurosurgeons on various other projects. These neurosurgeons have also provided guidance and advice on the presented work. The result of mutual discussions is also the need to integrate the HyTract method with fMRI functional studies done preoperatively. In this work, the interface between the white and gray matter of individual functional regions of the cerebral cortex, labeled based on functional atlases, was selected as the starting point for tracking. Ultimately, we intend to use the results of preoperative fMRI studies for this purpose, creating a comprehensive pipeline for preoperative connectivity studies for neurosurgeons.

Hybrid nature of this method allows for the potential use of its elements for other tasks related to brain diffusion. For instance, an ANN can be trained to detect crossing fiber points, which are of significant importance to neurosurgeons, as damaging them during surgery would disrupt connectivity with several cortical areas simultaneously. The ANN can be unaltered, and the A* algorithm can be replaced by other implementations, allowing further conclusions to be drawn regarding the white matter organization, such as connectivity studies between two regions of interest.

Despite the advantages of our approach, several limitations must be considered. While training with consensus tractograms helps reduce the number of false positives, it does not eliminate them entirely. Therefore, when constructing a tractogram, it is necessary to adjust the threshold value τ to obtain results suited to specific needs. Additionally, when processing substantially larger cube sizes (significantly exceeding the presented size of 9), it may be beneficial to use Dijkstra's algorithm for path reconstruction, as the A* algorithm's heuristic nature could lead to suboptimal results.

Furthermore, future work is needed to develop more robust similarity measures for tract comparison in consensus tractograms, and a more suitable heuristic function for A*. While Euclidean distance effectively captures the spatial relationship between points, it does not account for anatomical relevance, highlighting the need for improved distance metrics in future iterations of the method.

Notation and abbreviations

Table 5 summarizes the notation and abbreviations used in this article.

CRediT authorship contribution statement

Mateusz Korycinski: Writing – review & editing, Writing – original draft, Visualization, Validation, Software, Methodology, Investigation, Formal analysis, Data curation, Conceptualization. **Konrad A. Ciecierski:** Writing – review & editing, Writing – original draft, Supervision, Project administration, Methodology, Data curation, Conceptualization. **Ewa Niewiadomska-Szynkiewicz:** Writing – review & editing, Writing – original draft, Validation, Supervision, Resources, Project administration, Methodology, Investigation, Data curation, Conceptualization.

Declaration of competing interest

The authors declare that they have no known competing financial interests or personal relationships that could have appeared to influence the work reported in this paper.

Acknowledgments

Data were provided by the Human Connectome Project, WU-Minn Consortium (Principal Investigators: David Van Essen and Kamil Ugurbil; 1U54MH091657) funded by the 16 NIH Institutes and Centers that support the NIH Blueprint for Neuroscience Research; and by the McDonnell Center for Systems Neuroscience at Washington University.

We thank Dorota Mularczyk, PhD, and Antonina Krajewska, PhD, for their critical review and comments on the manuscript prior to submission.

We thank Tomasz Mandat, MD, PhD and Henryk Koziara, MD, PhD, from the Department of Neurosurgery in the National Oncology Center in Warsaw, Poland, for their consult on the medical matters of the project, as well as the future development and implementation in preoperative planning.

Data availability

Data will be made available on request.

References

Adnan, S. R., & Abdulbaqi, H. A. (2022). Deepfake video detection based on convolutional neural networks. In *2022 international conference on data science and intelligent computing* (pp. 65–69). http://dx.doi.org/10.1109/ICDSIC56987.2022.10075830.

Agnihotri, A., Saraf, P., & Bapnad, K. R. (2019). A convolutional neural network approach towards self-driving cars. In *2019 IEEE 16th India council international conference* (pp. 1–4). http://dx.doi.org/10.1109/INDICON47234.2019.9030307.

Al-Yasriy, H. F., Al-Husieny, M. S., Mohsen, F. Y., Khalil, E. A., & Hassan, Z. S. (2020). Diagnosis of lung cancer based on CT scans using CNN. *IOP Conference Series: Materials Science and Engineering*, *928*, Article 022035. http://dx.doi.org/10.1088/1757-899X/928/2/022035, https://iopscience.iop.org/article/10.1088/1757-899X/928/2/022035 https://iopscience.iop.org/article/10.1088/1757-899X/928/2/022035/meta.

Amunts, K., Malikovic, A., Mohlberg, H., Schormann, T., & Zilles, K. (2000). Brodmann's areas 17 and 18 brought into Stereotaxic space—Where and how variable? *NeuroImage*, *11*(1), 66–84. http://dx.doi.org/10.1006/nimg.1999.0516.

Amunts, K., Schleicher, A., Bürgel, U., Mohlberg, H., Uylings, H. B. M., & Zilles, K. (1999). Broca's region revisited: Cytoarchitecture and intersubject variability. *Journal of Comparative Neurology*, *412*(2), 319–341. http://dx.doi.org/10.1002/(SICI)1096-9861(19990920)412:2<319::AID-CNE10>3.0.CO;2-7.

Andersson, J. L. R., Jenkinson, M., & Smith, S. (2010). *Non-linear registration aka spatial normalisation FMRIB: FMRIB Technical Report TR07JA2*.

Aronis, C., Delibasis, K., Fanariotis, M., & Maglogiannis, I. (2016). A tractography algorithm for MR diffusion tensor imaging based on minimum-cost path. *IFMBE Proceedings*, *57*, 302–307. http://dx.doi.org/10.1007/978-3-319-32703-7{_}60/COVER.

Basser, P. J. (1998). Fiber-tractography via diffusion tensor MRI (DT-MRI). *Proceedings of the 6th Annual Meeting ISMRM*, *1*(January 1998), 3.

Basser, P. J., Mattiello, J., & LeBihan, D. (1994). MR diffusion tensor spectroscopy and imaging. *Biophysical Journal*, *66*(1), 259–267. http://dx.doi.org/10.1016/S0006-3495(94)80775-1.

Benou, I., & Riklin-Raviv, T. (2018). DeepTract: A probabilistic deep learning framework for white matter fiber tractography. *Lecture Notes in Computer Science (Including Subseries Lecture Notes in Artificial Intelligence and Lecture Notes in Bioinformatics): vol. 11766 LNCS*, (pp. 626–635). http://dx.doi.org/10.1007/978-3-030-32248-9{_}70.

Bukhari, H., Su, C., Dhamala, E., Gu, Z., Jamison, K., & Kuceyeski, A. (2022). A graph-matching based metric of functional connectome distance between pairs of individuals varies with their ages, cognitive performances and familial relationships. *BioRxiv*, http://dx.doi.org/10.1101/2022.10.03.510660, 2022.10.03.510660.

Chaichana, K. L., Jusue-Torres, I., Navarro-Ramirez, R., Raza, S. M., Pascual-Gallego, M., Ibrahim, A., et al. (2014). Establishing percent resection and residual volume thresholds affecting survival and recurrence for patients with newly diagnosed intracranial glioblastoma. *Neuro-Oncology*, *16*(1), 113–122. http://dx.doi.org/10.1093/NEUONC/NOT137.

Che, H., Brown, L. G., Foran, D. J., Nosher, J. L., & Hacihaliloglu, I. (2021). Liver disease classification from ultrasound using multi-scale CNN. *International Journal of Computer Assisted Radiology and Surgery*, *16*, 1537–1548. http://dx.doi.org/10.1007/S11548-021-02414-0/TABLES/4, URL https://link.springer.com/article/10.1007/s11548-021-02414-0.

Chou, Y.-l. (1969). Statistical analysis, with business and economic applications.. (p. 794). ISBN: 0030730953.

Christiaens, D., Reisert, M., Dhollander, T., Sunaert, S., Suetens, P., & Maes, F. (2015). Global tractography of multi-shell diffusion-weighted imaging data using a multi-tissue model. *NeuroImage*, *123*, 89–101. http://dx.doi.org/10.1016/J.NEUROIMAGE.2015.08.008.

Descoteaux, M., Deriche, R., Knösche, T. R., & Anwander, A. (2009). Deterministic and probabilistic tractography based on complex fibre orientation distributions. *IEEE Transactions on Medical Imaging*, *28*(2), 269–286. http://dx.doi.org/10.1109/TMI.2008.2004424.

Dijkstra, E. W. (1959). A note on two problems in connexion with graphs. *Numerische Mathematik*, *1*(1), 269–271. http://dx.doi.org/10.1007/BF01386390/METRICS.

Duffau, H. (2008). Brain plasticity and tumors.. *Advances and Technical Standards in Neurosurgery*, *33*, 3–33. http://dx.doi.org/10.1007/978-3-211-72283-1{_}1/COVER.

Feinberg, D. A., Moeller, S., Smith, S. M., Auerbach, E., Ramanna, S., Glasser, M. F., et al. (2010). Multiplexed echo planar imaging for sub-second whole brain FMRI and fast diffusion imaging. *PLOS ONE*, *5*(12), 1–11. http://dx.doi.org/10.1371/journal.pone.0015710.

Fonov, V., Evans, A. C., Botteron, K., Almli, C. R., McKinstry, R. C., & Collins, D. L. (2011). Unbiased average age-appropriate atlases for pediatric studies. *NeuroImage*, *54*(1), 313–327. http://dx.doi.org/10.1016/j.neuroimage.2010.07.033.

Fonov, V. S., Evans, A. C., McKinstry, R. C., Almli, C. R., & Collins, D. L. (2009). Unbiased nonlinear average age-appropriate brain templates from birth to adulthood. *NeuroImage*, *47*, S102. http://dx.doi.org/10.1016/S1053-8119(09)70884-5.

Foret, P., Kleiner, A., Mobahi, H., & Neyshabur, B. (2021). Sharpness-aware minimization for efficiently improving generalization. In *International conference on learning representations*.

Fornito, A., Zalesky, A., & Breakspear, M. (2013). Graph analysis of the human connectome: Promise, progress, and pitfalls. *NeuroImage*, *80*, 426–444. http://dx.doi.org/10.1016/J.NEUROIMAGE.2013.04.087.

Ganj, A., Ebadpour, M., Darvish, M., & Bahador, H. (2023). LR-net: A block-based convolutional neural network for low-resolution image classification. arXiv:2207.09531. URL https://arxiv.org/abs/2207.09531.

Garyfallidis, E. (2012). *Towards an accurate brain tractography* (Ph.D. thesis), University of Cambridge.

Garyfallidis, E., Brett, M., Amirbekian, B., Rokem, A., Van Der Walt, S., Descoteaux, M., et al. (2014). Dipy, a library for the analysis of diffusion MRI data. *Frontiers in Neuroinformatics*, *8*.

Garyfallidis, E., Koudoro, S., Guaje, J., Côté, M.-A., Biswas, S., Reagan, D., et al. (2021). FURY: advanced scientific visualization. *Journal of Open Source Software*, *6*(64), 3384. http://dx.doi.org/10.21105/JOSS.03384.

Goodfellow, I., Bengio, Y., & Courville, A. (2016). *Deep Learning*. MIT Press.

Greve, D. N., & Fischl, B. (2009). Accurate and robust brain image alignment using boundary-based registration. *NeuroImage*, *48*(1), 63–72. http://dx.doi.org/10.1016/j.neuroimage.2009.06.060.

Hagmann, P., Jonasson, L., Maeder, P., Thiran, J. P., Wedeen, J. V., & Meuli, R. (2006). Understanding diffusion MR imaging techniques: From scalar diffusion-weighted imaging to diffusion tensor imaging and Beyond1. *26*(SPEC. ISS.), http://dx.doi.org/10.1148/RG.26SI065510.

Harris, C. R., Millman, K. J., van der Walt, S. J., Gommers, R., Virtanen, P., Cournapeau, D., et al. (2020). Array programming with numpy. *Nature*, *585*(7825), 357–362. http://dx.doi.org/10.1038/s41586-020-2649-2.

Hart, P. E., Nilsson, N. J., & Raphael, B. (1968). A formal basis for the heuristic determination of minimum cost paths. *IEEE Transactions on Systems Science and Cybernetics*, *4*(2), 100–107. http://dx.doi.org/10.1109/TSSC.1968.300136.

Hunter, J. D. (2007). Matplotlib: A 2D graphics environment. *Computing in Science and Engineering*, *9*(3), 90–95. http://dx.doi.org/10.1109/MCSE.2007.55.

Jenkinson, M., Bannister, P., Brady, M., & Smith, S. (2002). Improved optimization for the robust and accurate linear registration and motion correction of brain images. *NeuroImage*, *17*(2), 825–841. http://dx.doi.org/10.1006/nimg.2002.1132.

Jenkinson, M., Beckmann, C. F., Behrens, T. E. J., Woolrich, M. W., & Smith, S. M. (2012). FSL. *NeuroImage*, *62*(2), 782–790. http://dx.doi.org/10.1016/j.neuroimage.2011.09.015.

Jenkinson, M., Pechaud, M., & Smith, S. (2005). BET2: MR-based estimation of brain, skull and scalp surfaces. In *Eleventh annual meeting of the organization for human brain mapping*.

Jenkinson, M., & Smith, S. (2001). A global optimisation method for robust affine registration of brain images. *Medical Image Analysis*, *5*(2), 143–156. http://dx.doi.org/10.1016/S1361-8415(01)00036-6.

Kingma, D. P., & Ba, J. (2017). Adam: A method for stochastic optimization. http://dx.doi.org/10.48550/arXiv.1412.6980, arXiv:1412.6980.

Krogh, A., & Hertz, J. A. (1991). A simple weight decay can improve generalization. In *Proceedings of the 4th international conference on neural information processing systems* (pp. 950–957). San Francisco, CA, USA: Morgan Kaufmann Publishers Inc..

Kwon, J., Kim, J., Park, H., & Choi, I. K. (2021). ASAM: Adaptive sharpness-aware minimization for scale-invariant learning of deep neural networks. (pp. 5905–5914).

Lazar, M., Weinstein, D. M., Tsuruda, J. S., Hasan, K. M., Arfanakis, K., Meyerand, M. E., et al. (2003). White matter tractography using diffusion tensor deflection. *Human Brain Mapping*, *18*(4), 306–321. http://dx.doi.org/10.1002/hbm.10102.

Li, S. C. (2013). The difficulty of protein structure alignment under the RMSD. *Algorithms for Molecular Biology*, *8*, 1–9. http://dx.doi.org/10.1186/1748-7188-8-1/TABLES/4, URL https://almob.biomedcentral.com/articles/10.1186/1748-7188-8-1.

Logothetis, N. K., Pauls, J., Augath, M., Trinath, T., & Oeltermann, A. (2001). Neurophysiological investigation of the basis of the fMRI signal. *Nature*, *412*(68436843), 150–157. http://dx.doi.org/10.1038/35084005.

Luján, M. Á., Jimeno, M. V., Mateo Sotos, J., Ricarte, J. J., & Borja, A. L. (2021). A survey on EEG signal processing techniques and machine learning: Applications to the neurofeedback of autobiographical memory deficits in schizophrenia. *Electronics*, *10*(23), http://dx.doi.org/10.3390/electronics10233037, URL https://www.mdpi.com/2079-9292/10/23/3037.

McCarthy, P. (2023). Fsleyes. http://dx.doi.org/10.5281/zenodo.10122614.

Mehrnia, M., Kholmovski, E., Katsaggelos, A., Kim, D., Passman, R., & Elbaz, M. S. (2024). Novel self-calibrated threshold-free probabilistic fibrosis signature technique for 3D late gadolinium enhancement MRI. *IEEE Transactions on Biomedical Engineering*, http://dx.doi.org/10.1109/TBME.2024.3476930.

Milletari, F., Ahmadi, S.-A., Kroll, C., Plate, A., Rozanski, V., Maiostre, J., et al. (2017). Hough-CNN: Deep learning for segmentation of deep brain regions in mri and ultrasound. *Computer Vision and Image Understanding*, *164*, 92–102. http://dx.doi.org/10.1016/j.cviu.2017.04.002, URL https://www.sciencedirect.com/science/article/pii/S1077314217300620, Deep Learning for Computer Vision.

Moeller, S., Yacoub, E., Olman, C. A., Auerbach, E., Strupp, J., Harel, N., et al. (2010). Multiband multislice GE-EPI at 7 tesla, with 16-fold acceleration using partial parallel imaging with application to high spatial and temporal whole-brain fMRI. *Magnetic Resonance in Medicine*, *63*(5), 1144–1153. http://dx.doi.org/10.1002/mrm.22361.

Neher, P. F., Côté, M. A., Houde, J. C., Descoteaux, M., & Maier-Hein, K. H. (2017). Fiber tractography using machine learning. *NeuroImage*, *158*, 417–429. http://dx.doi.org/10.1016/J.NEUROIMAGE.2017.07.028.

Neher, P. F., Götz, M., Norajitra, T., Weber, C., & Maier-Hein, K. H. (2015). A machine learning based approach to fiber tractography using classifier voting. *Lecture notes in computer science (including subseries lecture notes in artificial intelligence and lecture notes in bioinformatics)*: *vol. 9349*, (pp. 45–52). http://dx.doi.org/10.1007/978-3-319-24553-9{_}6/COVER.

Paszke, A., Gross, S., Massa, F., Lerer, A., Bradbury, J., Chanan, G., et al. (2019). Pytorch: An imperative style, high-performance deep learning library. *Advances in Neural Information Processing Systems*, *32*.

Pooley, R. A. (2005). Fundamental physics of MR imaging. *Radiographics*, *25*(4), 1087–1099. http://dx.doi.org/10.1148/RG.254055027.

Poulin, P., Côté, M.-A., Houde, J.-C., Petit, L., Neher, P. F., Maier-Hein, K. H., et al. (2017). Learn to track: Deep learning for tractography. *BioRxiv*, Article 146688. http://dx.doi.org/10.1101/146688.

Poulin, P., Rheault, F., St-Onge, E., Jodoin, P.-M., & Descoteaux, M. (2018). Bundle-wise deep tracker: Learning to track bundle-specific streamline paths. In *Proceedings of the international society for magnetic resonance in medicine ISMRM-ESMRMB*.

Przybylowski, C. J., Hervey-Jumper, S. L., & Sanai, N. (2021). Surgical strategy for insular glioma. *Journal of Neuro-Oncology*, *151*, 491–497. http://dx.doi.org/10.1007/S11060-020-03499-4/FIGURES/3, URL https://link.springer.com/article/10.1007/s11060-020-03499-4.

Reisert, M., Mader, I., Anastasopoulos, C., Weigel, M., Schnell, S., & Kiselev, V. (2011). Global fiber reconstruction becomes practical. *NeuroImage*, *54*(2), 955–962. http://dx.doi.org/10.1016/J.NEUROIMAGE.2010.09.016.

Robbins, H. E. (2007). A stochastic approximation method. *Annals of Mathematical Statistics*, *22*, 400–407.

Sanai, N., Polley, M. Y., McDermott, M. W., Parsa, A. T., & Berger, M. S. (2011). An extent of resection threshold for newly diagnosed glioblastomas: Clinical article. *Journal of Neurosurgery*, *115*(1), 3–8. http://dx.doi.org/10.3171/2011.2.JNS10998.

Setsompop, K., Gagoski, B. A., Polimeni, J. R., Witzel, T., Wedeen, V. J., & Wald, L. L. (2012). Blipped-controlled aliasing in parallel imaging for simultaneous multislice echo planar imaging with reduced g-factor penalty. *Magnetic Resonance in Medicine*, *67*(5), 1210–1224. http://dx.doi.org/10.1002/mrm.23097.

Seydi, S. T., Boueshagh, M., Namjoo, F., Minouei, S. M., Nikraftar, Z., & Amani, M. (2024). A hyperspectral change detection (HCD-Net) framework based on double stream convolutional neural networks and an attention module. *Remote Sensing*, *16*(5), http://dx.doi.org/10.3390/rs16050827, URL https://www.mdpi.com/2072-4292/16/5/827.

Singleton, M. J. (2009). Functional magnetic resonance imaging. *The Yale Journal of Biology and Medicine*, *82*(4), 233.

Smith, S. M. (2002). Fast robust automated brain extraction. *Human Brain Mapping*, *17*(3), 143–155. http://dx.doi.org/10.1002/hbm.10062.

Smith, S. M., Jenkinson, M., Woolrich, M. W., Beckmann, C. F., Behrens, T. E. J., Johansen-Berg, H., et al. (2004). Advances in functional and structural MR image analysis and implementation as FSL. *NeuroImage*, *23*, S208–S219. http://dx.doi.org/10.1016/j.neuroimage.2004.07.051.

Smith, R. E., Tournier, J.-D., Calamante, F., & Connelly, A. (2012). Anatomically-constrained tractography: Improved diffusion mri streamlines tractography through effective use of anatomical information. *NeuroImage*, *62*(3), 1924–1938. http://dx.doi.org/10.1016/j.neuroimage.2012.06.005.

Sotiropoulos, S. N., Bai, L., Morgan, P. S., Constantinescu, C. S., & Tench, C. R. (2010). Brain tractography using Q-ball imaging and graph theory: Improved connectivities through fibre crossings via a model-based approach. *NeuroImage*, *49*(3), 2444–2456. http://dx.doi.org/10.1016/J.NEUROIMAGE.2009.10.001.

Tournier, J. D., Calamante, F., & Connelly, A. (2007). Robust determination of the fibre orientation distribution in diffusion MRI: Non-negativity constrained super-resolved spherical deconvolution. *NeuroImage*, *35*(4), 1459–1472. http://dx.doi.org/10.1016/J.NEUROIMAGE.2007.02.016.

Tournier, J. D., Calamante, F., & Connelly, A. (2012). MRtrix: Diffusion tractography in crossing fiber regions. *International Journal of Imaging Systems and Technology*, *22*(1), 53–66. http://dx.doi.org/10.1002/IMA.22005.

Tournier, J.-D., Smith, R., Raffelt, D., Tabbara, R., Dhollander, T., Pietsch, M., et al. (2019). MRtrix3: A fast, flexible and open software framework for medical image processing and visualisation. *NeuroImage*, *202*, Article 116137. http://dx.doi.org/10.1016/j.neuroimage.2019.116137.

Tuch, D. S. (2004). Q-ball imaging. *Magnetic Resonance in Medicine*, *52*(6), 1358–1372. http://dx.doi.org/10.1002/MRM.20279.

Van Essen, D. C., Ugurbil, K., Auerbach, E., Barch, D., Behrens, T. E. J., Bucholz, R., et al. (2012). The human connectome project: A data acquisition perspective. *NeuroImage*, *62*(4), 2222–2231. http://dx.doi.org/10.1016/j.neuroimage.2012.02.018.

Vanderach, T. W., & Gould, D. J. (2016). *Nolte's the human brain: an introduction to its functional anatomy*. Elsevier.

Wilson, A. C., Roelofs, R., Stern, M., Srebro, N., & Recht, B. (2017). The marginal value of adaptive gradient methods in machine learning. *Advances in Neural Information Processing Systems*, *2017-December*, 4149–4159.

Woolrich, M. W., Jbabdi, S., Patenaude, B., Chappell, M., Makni, S., Behrens, T., et al. (2009). Bayesian analysis of neuroimaging data in FSL. *NeuroImage*, *45*(1 Suppl), 173–186. http://dx.doi.org/10.1016/j.neuroimage.2008.10.055.

Xu, J., Moeller, S., Strupp, J., Auerbach, E. J., Chen, L., Feinberg, D. A., et al. (2012). Highly accelerated whole brain imaging using aligned-blipped-controlled-aliasing multiband EPI. (p. 1).

Yektaeian Vaziri, A., Makkiabadi, B., & Samadzadehaghdam, N. (2023). EEGg: Generating synthetic EEG signals in Matlab environment. *Frontiers in Biomedical Technologies*, *10*(3), 370–381. http://dx.doi.org/10.18502/fbt.v10i3.13165, URL https://fbt.tums.ac.ir/index.php/fbt/article/view/590.

Yousefi, O., Azami, P., Sabahi, M., Dabecco, R., Adada, B., & Borghei-Razavi, H. (2022). Management of optic pathway Glioma: A systematic review and meta-analysis. *Cancers*, *14*(19), http://dx.doi.org/10.3390/cancers14194781, URL https://www.mdpi.com/2072-6694/14/19/4781.

Zalesky, A. (2008). DT-MRI fiber tracking: A shortest paths approach. *IEEE Transactions on Medical Imaging*, *27*(10), 1458–1471. http://dx.doi.org/10.1109/TMI.2008.923644.